

Radio Interferometric Studies of Cool Evolved Stellar Outflows

A dissertation submitted to the University of Dublin
for the degree of Doctor of Philosophy

Eamon O’Gorman

Supervisor: Dr. Graham M. Harper

Trinity College Dublin, September 2013

SCHOOL OF PHYSICS
UNIVERSITY OF DUBLIN
TRINITY COLLEGE



Declaration

I declare that this thesis has not been submitted as an exercise for a degree at this or any other university and it is entirely my own work.

I agree to deposit this thesis in the University's open access institutional repository or allow the library to do so on my behalf, subject to Irish Copyright Legislation and Trinity College Library conditions of use and acknowledgement.

Name: Your Name

Signature: **Date:**

Summary

You should write a nice summary here...

A dedication if you wish...

Acknowledgements

Some sincere acknowledgements...

List of Publications

Refereed

1. **O’Gorman, E.**, Harper, G. M., Brown, J. M., Brown, A., Redfield, S., Richter, M. J., and Requena-Torres, M. A.
“CARMA CO(J = 2 - 1) Observations of the Circumstellar Envelope of Betelgeuse”
The Astronomical Journal, 144, 36 (2012)
2. Sada, P. V., Deming, D., Jennings, D. E., Jackson, B. K., Hamilton, C. M., Fraine, J., Peterson, S. W., Haase, F., Bays, K., Lunsford, A., and **O’Gorman, E.**
“Extrasolar Planet Transits Observed at Kitt Peak National Observatory”
Publications of the Astronomical Society of the Pacific, 124, 212 (2012)
3. Sada, P. V., Deming, D., Jackson, B. K., Jennings, D. E., Peterson, S. W., Haase, F., Bays, K., **O’Gorman, E.**, and Lundsford, A.
“Recent Transits of the Super-Earth Exoplanet GJ 1214b”
The Astrophysical Journal Letters, 720, L215 (2010)

Non-Refereed

1. **O’Gorman, E.**, & Harper, G. M.
“What is Heating Arcturus’ Wind?”,
Proceedings of the 16th Cambridge Workshop on Cool Stars, Stellar Systems and the Sun. Astronomical Society of the Pacific Conference Series, 448, 691 (2011)

Contents

List of Publications	vi
List of Figures	ix
List of Tables	x
1 Introduction	1
1.1 First Section	1
1.2 Second Section	1
1.3 Second Section	2
2 Introduction to Radio Interferometry	3
2.1 Radio Antenna Fundamentals	3
2.1.1 Properties of a Radio Antenna	4
2.1.2 Antenna Structural Design	7
2.1.3 Antenna Performance Parameters	9
2.2 Receiving System for an Interferometer	11
2.3 Fundamentals of Radio Interferometry	13
2.3.1 Young’s Slits	13
2.3.2 The Two-element Interferometer	15
2.3.3 Complex Visibility	19
2.3.4 Coordinate Systems for Imaging	20
2.4 Synthesis Imaging	21
2.4.1 Visibility Sampling	21
2.4.2 Imaging (Making a Dirty Map)	22
2.4.3 Deconvolution (Making a CLEAN map)	25

3	Targets, Instrumentation, and Observations	28
3.1	Betelgeuse	28
3.2	CARMA	28
3.3	CARMA Observations of Betelgeuse	28
3.4	Arcturus and Aldebaran	31
3.5	The Karl G. Jansky Very Large Array	36
3.6	VLA Observations of Arcturus and Aldebaran	39
4	Data Analysis	46
4.1	Measurement Equation	46
5	CARMA CO($J = 2 - 1$) Observations of the Circumstellar Envelope of Betelgeuse	47
5.1	Introduction	47
6	Multi-wavelength Radio Continuum Emission Studies of Dust-free Red Giants	48
6.1	Introduction	48
6.2	α Boo Radio Maps	48
6.3	α Tau Radio Maps	48
6.4	Results vs Previous Observations	48
6.5	Results vs Existing Models	50
6.6	Constraining α Tau's Molsphere	50
6.7	Estimation of Mass Loss Rates from the Radio Data	51
6.8	Spectral Indices	52
6.9	Analytical Advection Model for α Boo's Wind	59
6.9.1	H II recombination in a stellar outflow	59
6.9.2	Application to α Boo's Wind	61
A	A Nice Appendix	65
	References	66

List of Figures

1.1	Red Giant and Asymptotic Giant Branch Stars	2
2.1	Radiation and power pattern of a uniformly illuminated antenna.	6
2.2	Common optical systems used for radio antennas.	9
2.3	Block diagram of a superheterodyne receiver.	12
2.4	Fringe pattern produced by Young's slits under various situations.	14
2.5	Visibilities for various source sizes.	16
2.6	Simplified schematic diagram of a two-element interferometer. . .	17
2.7	The instantaneous point source responses of an interferometer. . .	18
2.8	The (u, v, w) interferometric coordinate system.	22
2.9	VLA antenna layout and two examples of $u - v$ coverage for dif- ferent track lengths.	23
2.10	The Fourier transform pairs in synthesis imaging.	24
3.1	Main features of a VLA antenna.	39
3.2	Importance of offsetting source from phase center.	43
3.3	Overview of a low and high frequency VLA observation.	45
6.1	Power law fits to the spectra of α Boo and α Tau.	55
6.2	Variation of density and temperature coefficients for α Boo and α Tau.	56
6.3	Predicted effective radius as a function of wavelength for α Boo and α Tau.	58
6.4	The temperature dependent recombination rates for hydrogen. . .	63
6.5	Hybrid Drake model which undergoes rapid wind cooling beyond $\sim 2.3 R_{\star}$	64

List of Tables

3.1	Physical Properties of α Ori.	29
3.2	CARMA Observations of α Ori.	30
3.3	Basic Properties of α Boo and α Tau.	33
3.4	Improved Performance Parameters of the VLA.	37
3.5	Frequency coverage, primary beam, and angular resolution of the VLA.	40
3.6	VLA Observations of α Boo and α Tau.	41
6.1	Compilation of Previous Radio Observations ($\nu \leq 250$ GHz). . . .	49
6.2	Ionized mass loss rates for α Boo and α Tau.	52

1

Introduction

Here is the introduction of the thesis, complete with a few references ([Prothero & Buell, 2007](#); [Sagan, 1997](#)). Section [1.1](#) contains Equation [1.1](#), Section [1.2](#) has Figure [1.1](#) and Section [2.3](#) has Table [3.6](#). Chapter [2](#) has pretty much nothing in it.

1.1 First Section

This section has an equation. Here it is:

$$L_{\odot} = 4\pi R_{\odot}^2 \sigma T_e^4 \tag{1.1}$$

which is a nice way of describing the luminosity.

1.2 Second Section

So this section has a figure in it^{[1](#)}. That figure depicts the basic structure of a red giant.

¹And also a footnote.

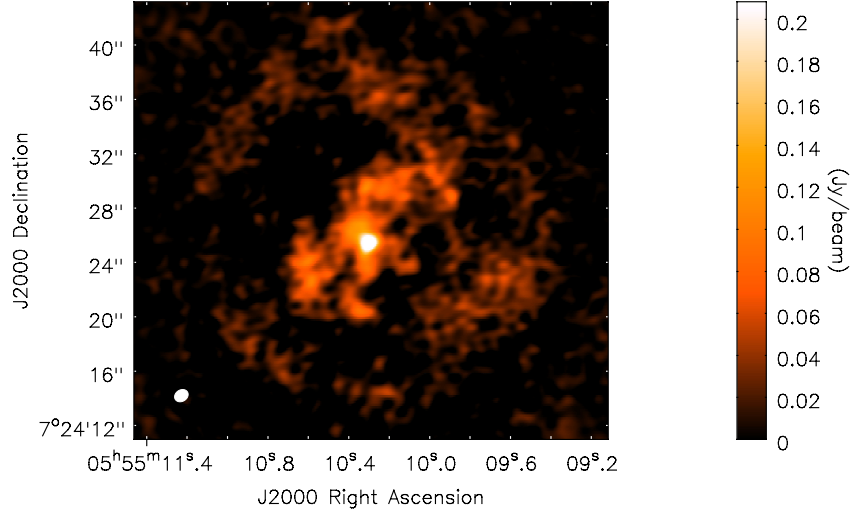


Figure 1.1: Red Giant and Asymptotic Giant Branch Stars. The left side of the figure shows the basic structure of a star on the giant branch of the HR diagram, while the right side shows a similar star after it has evolved to ascend the asymptotic giant branch. *Image Credit: Australian Telescope National Facility.*

1.3 Second Section

2

Introduction to Radio Interferometry

The poor spatial resolution provided by a single dish radio antenna can cause difficulties in obtaining accurate flux density measurements of radio astronomical sources, especially at long wavelengths. A single dish radio antenna is unable to distinguish against background radio emitters located in the primary beam, and therefore the observed flux density can contain emission from unrelated sources. This limitation can be overcome through interferometry. An interferometer acts as a spatial filter, and can discriminate against smooth backgrounds, while its higher resolution allows separation of the target from nearby confusing sources. This chapter describes the basic elements of a radio interferometer, what happens to the radio signal before it is sent for correlation, introduces the general concept of interferometry, and explains the process of synthesis imaging.

2.1 Radio Antenna Fundamentals

The quality and properties of the final radio image produced from a synthesis array are partially dependent on the properties of the individual antennas in the array. The most important such properties are discussed in the following sections and include aperture size, aperture efficiency, pointing accuracy and sidelobe

level. We define the radio antenna as the piece of equipment which converts the electromagnetic waves emitted from the observed source into an electric current ready to be input into the first low noise amplifier where the signal is at the radio/sky frequency, ν_{RF} . What happens to the signal after this will be discussed in Section 2.2.

2.1.1 Properties of a Radio Antenna

The power gain of a transmitting antenna is a measure of the antenna's capability of converting power into radio waves in a specific direction. In radio astronomy, the receiving counterpart of transmitting power gain is the effective collecting area of an antenna, $A(\nu, \theta, \phi)$, where ν is frequency and θ and ϕ are direction coordinates. An ideal radio antenna would collect all incident radiation from a distant point source and convert it to electrical power. The total spectral power P_ν collected by it would then be a product of its geometric area and the incident spectral power per area, or flux density F_ν . By analogy then, the effective area of a real radio antenna is defined

$$A(\nu, \theta, \phi) = \frac{P_\nu}{F_\nu} = \frac{P}{I(\nu, \theta, \phi) \Delta\nu \Delta\Omega} \quad (2.1)$$

where $I(\nu, \theta, \phi)$ is the source brightness in units $\text{W m}^{-2} \text{Hz}^{-1} \text{sr}^{-1}$ that the antenna is pointing at and P is the power (in Watts) received by the antenna in bandwidth $\Delta\nu$ from element $\Delta\Omega$ of solid angle. The normalized antenna reception pattern \mathcal{A} , often referred to as the power pattern due to the duality between receiving and transmitting, is defined as

$$\mathcal{A}(\nu, \theta, \phi) = \frac{A(\nu, \theta, \phi)}{A_0} \quad (2.2)$$

where A_0 (m^2) is often referred to as the effective area of the antenna and is the response at the center of the main lobe of $A(\nu, \theta, \phi)$ [i.e., $A(\nu, 0, 0)$]. Then the beam solid angle, Ω_A , of the primary beam is

$$\Omega_A = \iint_{\text{all sky}} \mathcal{A}(\theta, \phi) d\Omega \quad (2.3)$$

and is a measure of the field of view of the antenna.

2.1 Radio Antenna Fundamentals

In the case of an isotropic antenna [i.e., $\mathcal{A}(\nu, \theta, \phi) = 1$], it can be shown that the product of the effective area and the primary beam solid angle is equal to the square of the wavelength (Kraus *et al.*, 1986)

$$A_0 \Omega_A = \lambda^2. \quad (2.4)$$

Ω_A has its maximum possible value of 4π if \mathcal{A} is everywhere equal to 1. This means that the primary antenna can see the whole sky with equal sensitivity. Even though a large field of view is usually desirable in radio astronomy, Equation 2.4 ensures that for any given wavelength, when Ω_A is a maximum, the power received is a minimum and therefore the sensitivity is also at a minimum. To improve sensitivity, one could increase the collecting area of the antenna, but Equation 2.4 then ensures that the field of view must decrease. Thus, when deciding on the primary antenna size in a synthesis array, there is always a trade-off between field of view and sensitivity.

In reality, an antenna cannot radiate isotropically and will radiate preferentially in one or more directions. A Fourier transform relationship exists between the complex voltage distribution of the field, $f(u, v)$, in the aperture of the antenna and the complex far-field voltage radiation pattern, $F(l, m)$, of the antenna (Kraus *et al.*, 1986)

$$F(l, m) = \iint_{\text{aperture}} f(u, v) e^{2\pi i(ul+vm)} du dv \quad (2.5)$$

and

$$f(u, v) = \int_{-\infty}^{\infty} \int_{-\infty}^{\infty} F(l, m) e^{-2\pi i(ul+vm)} dl dm \quad (2.6)$$

where

$$u = \sin\theta\cos\phi \quad \text{and} \quad v = \sin\theta\sin\phi \quad (2.7)$$

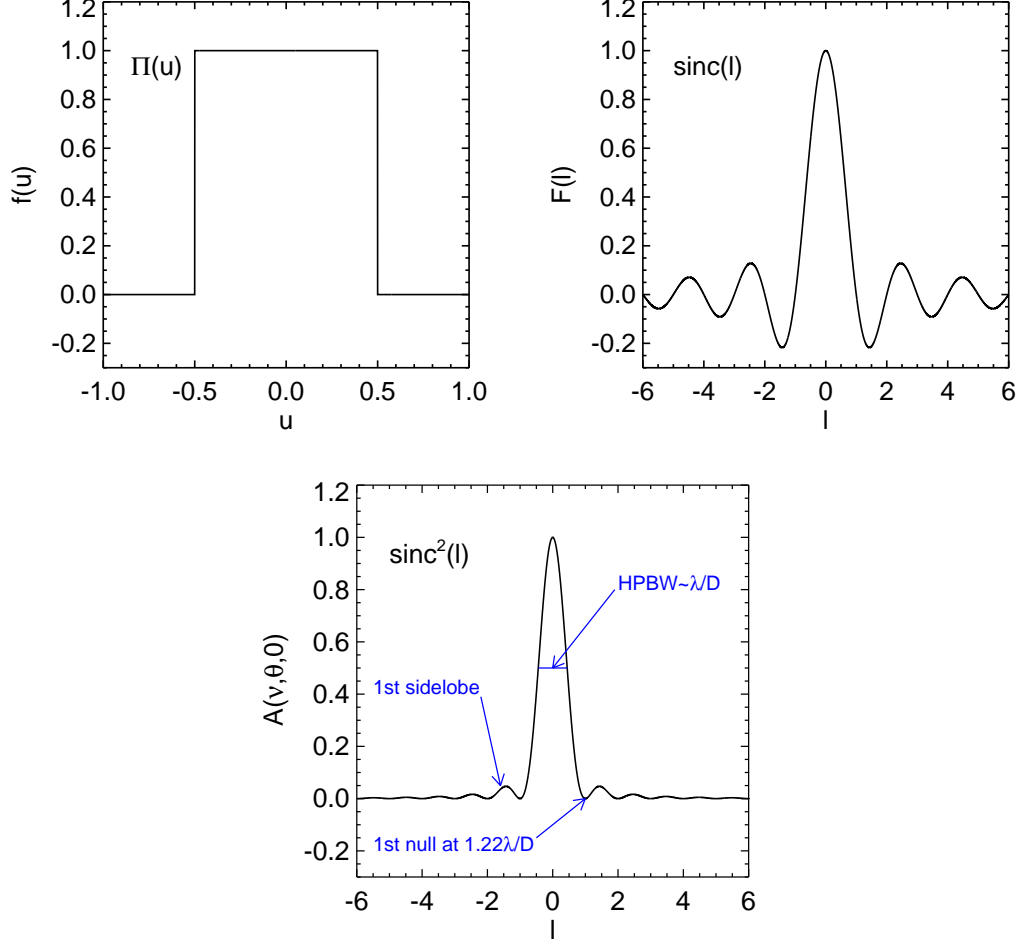


Figure 2.1: *Top Left:* A uniformly illuminated 1-D aperture $f(u)$. *Top Right:* The Fourier transform of $f(u)$ gives the antenna radiation pattern in the far-field, $F(l)$. *Bottom:* The power pattern of the antenna is given by $\mathcal{A} = |F(l)|^2$.

are the antenna coordinates and l and m are their Fourier counterparts. The form of $f(u, v)$ is determined by the manner in which the antenna feed illuminates the aperture. Therefore Equations 2.6 and 2.7 tell us that the radiation pattern in the far-field of a two-dimensional aperture is the two-dimensional Fourier transform of the aperture field illumination. For a uniformly illuminated 1-D aperture shown in Figure 2.1, the radiation pattern in the far-field is the *sinc* function. The radiation pattern in the far-field, $F(l, m)$, of such an antenna is related to the antenna power pattern by $\mathcal{A} = |F(l, m)|^2$. This power pattern is known as the Airy pattern if the antenna is uniformly illuminated and is also shown in Figure

2.1. The central peak of this power pattern is called the main beam while the smaller secondary peaks are called sidelobes. The antenna is maximally sensitive to radiation from the direction of the peak of the beam, but is also slightly sensitive to radiation in the direction of the side lobes. The half-power beamwidth (HPBW) of the main beam θ_{HPBW} is a term commonly used in the literature to describe the field of view of an antenna/interferometer and satisfies

$$\theta_{\text{HPBW}} \propto \frac{\lambda}{D} \quad (2.8)$$

where D is the diameter of the antenna. The constant of proportionality varies slightly with the illumination taper and can be shown to be equal to ~ 0.89 for a uniformly illuminated 1-D aperture and ~ 1.2 for most single dish radio antennas. When the sky is scanned with a single dish antenna, then this HPBW is the resolution of the resulting map.

2.1.2 Antenna Structural Design

The design of the primary antenna element of an interferometric array will depend on the wavelength range to be observed. In general, dipoles are used for wavelengths longer than ~ 1 m, while reflector antennas are typically used at shorter wavelengths. The reason why the more simple and less expensive dipoles are not used at all wavelengths is given by Equation 2.4. For an isotropic antenna, this equation tells us that the effective area is just

$$A_0 = \frac{\lambda^2}{4\pi}. \quad (2.9)$$

Therefore, at short wavelengths a non-directional antenna such as a dipole, will have a small effective collecting area, giving it poor sensitivity for reception. Thus, dipoles can be used at long wavelengths as they have sufficient collecting area, but cannot be used at shorter wavelengths as an impractical amount would be needed to produce useful collecting areas. Since the interferometric arrays used in this thesis use reflector antennas, the rest of this section will focus on them.

2.1 Radio Antenna Fundamentals

Choice of Antenna Mount. Nearly all interferometric arrays consist of antennas which have altitude over azimuth (alt-azimuth) mounts. These antennas lie on a horizontal azimuth track on which the antenna can turn in azimuth, and on a horizontal elevation axle about which the antenna can change in zenith angle. The main advantage of such a design is simplicity and thus lower cost. Gravity always acts on the reflector in the same plan thus reducing the problem of keeping the reflector profile accurate during the duration an observation. However, sources close to the zenith can usually not be observed due to the high rate of azimuth rotation required. Also, the beam rotates with respect to the source for long duration observations which can affect the dynamic range of total intensity images of very large sources. The other type of mount occasionally used is the equatorial mount. Its polar axis is aligned parallel to the axis of rotation of the Earth and therefore only needs to rotate about the declination axis to observe a source. Its beam also doesn't have the beam rotation problem encountered by the alt-azimuth design and can track sources close to the zenith. Its major disadvantage and the reason for its scarce usage is the complexity of its design and resulting increased cost.

Choice of Antenna Optics. In Figure 2.2 we show the main optical systems which can be used to feed a large radio reflector. The prime focus system (e.g. used in the Giant Meter Radio Telescope) has the advantage that it can be used at long wavelengths where the use of secondary focus feeds (i.e., sub-reflectors) become impractical. However, access to and space for the feeds and receivers are limited, and sensitivity can be lost due to spillover noise from the ground. The other designs have the advantage of easier access to the feeds and receivers and less spillover noise from the ground. The off-axis Cassegrain (e.g. used in the Very Large Array) also has the advantage of increased frequency capability as many feeds can be located in a circle around the center of the reflector and a slight rotation of the sub-reflector is all that is required to change observing frequency. The receivers and feeds in the Naysmith geometry (e.g. used in the Combined Array for Research in Millimeter wave Astronomy) are located externally to the antenna structure. Finally, the offset Cassegrain (e.g. used in the Green Bank Telescope)

has no blockage and will have a circularly symmetric beam with low sidelobes although the increase complexity of its structure leads to increased costs.

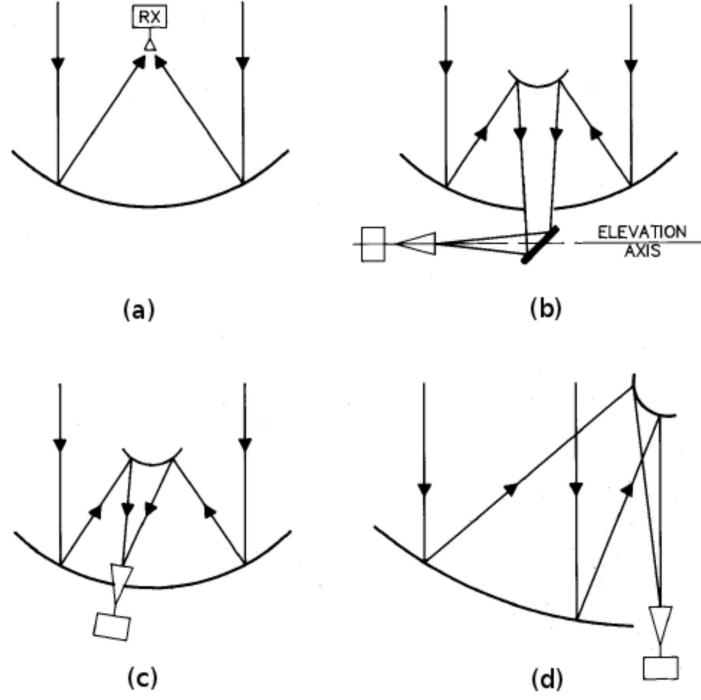


Figure 2.2: Common optical systems used for radio antennas. (a) Prime focus, (b) Naysmith, (c) Off-axis Cassegrain, (d) Offset Cassegrain [Figure adapted from Taylor *et al.* (1999)].

2.1.3 Antenna Performance Parameters

Aperture Efficiency. The geometric collecting area of a parabolic antenna A_{geo} ($= \pi D^2/4$) is related to the effective area (i.e., the collecting area when pointing directly at a source) via the dimensionless quantity η ($\eta < 1$) known as the aperture efficiency where

$$\eta = \frac{A_0}{A_{\text{geo}}}. \quad (2.10)$$

The aperture efficiency directly impacts on the sensitivity of the interferometric array and can be defined as the product of a number of different efficiency loss

factors,

$$\eta = \eta_{\text{sf}}\eta_{\text{bl}}\eta_{\text{s}}\eta_{\text{t}}\eta_{\text{misc}}. \quad (2.11)$$

The surface efficiency η_{sf} accounts for the aperture efficiency loss as a result of reflector profile inaccuracies. Such inaccuracies result in the electric field from various parts of the aperture not adding together in phase at the feed leading to a decrease in power. The aperture blockage efficiency η_{bl} accounts for the fact that the sub-reflector (or feed) and its support structure result in a reduction in the incident radiation on the antenna. The feed spillover efficiency η_{bl} is best understood if the antenna is considered in transmission rather than in reception mode, and is defined as the fraction of power radiated by the feed that is intercepted by the reflector for a prime focus system, or by the sub-reflector for a Cassegrain system. The illumination taper efficiency η_{t} accounts for the fact that the feed pattern does not illuminate the primary reflector uniformly but illuminates the outer part of the reflector at a lower level than the inner part. Finally, the miscellaneous efficiency losses such as reflector diffraction and feed position phase errors are accounted for in η_{misc} . As an example, the total aperture efficiency of the VLA antennas can vary between 0.65 and 0.2 at 6 and 0.7 cm, respectively.

Pointing Accuracy. The main lobe of an antenna's power pattern will usually not point exactly in the desired direction due to gravity deformations, wind pressure deformations, and mechanical inaccuracy. The angular offset, $\Delta\theta$, between the actual and desired pointing direction is called the pointing error. Usually, the desirable pointing error of an antenna at the highest operational frequency is $\Delta\theta < \theta_{\text{HPBW}}/20$ (Taylor *et al.*, 1999). With this specification reached, an antenna pointing at a compact source will suffer negligible intensity variations as $\mathcal{A}(\theta_{\text{HPBW}}/20) > 0.99$. However, this pointing error of only $\theta_{\text{HPBW}}/20$ will still have a substantial effect on the accuracy of the outer image. For example, a source located at the half power point will suffer a substantial fractional intensity variation of $2\mathcal{A}(\theta_{\text{HPBW}}/2 + \theta_{\text{HPBW}}/20) \simeq 0.86$. The blind pointing of a VLA antenna is only about $10''$ and can be much worse in daytime, occasionally exceeding $1'$. This means that at Q-band (45 GHz; 0.7 cm), which is the highest observing frequency on the VLA, the pointing error is only at best $\theta_{\text{HPBW}}/6$, and

at worst $> \theta_{\text{HPBW}}$, meaning that the target may lie outside of the primary beam. To overcome this problem of large antenna pointing errors at high frequencies with the VLA, a technique known as referenced pointing is implemented. This technique will be discussed further in Chapter 3.

2.2 Receiving System for an Interferometer

A radiometer (a radio receiver) is a device used to measure the timed-averaged power of the noise coming from a radio telescope within a well-defined radio frequency (RF) range, $\nu_{\text{RF}} - \Delta\nu_{\text{RF}}/2 \rightarrow \nu_{\text{RF}} + \Delta\nu_{\text{RF}}/2$, where $\Delta\nu_{\text{RF}}$ is the bandwidth of the receiver and $\Delta\nu_{\text{RF}} < \nu_{\text{RF}}$. The simplest radiometer carries out the following tasks:

1. Filters the broadband noise coming from the antenna via a bandpass filter.
2. Multiplies the filtered voltage by itself (i.e., its output voltage is proportional to its input power).
3. Smooths out the rapidly fluctuating output of the detected voltage via a signal averager or integrator.
4. Measures the smoothed voltage.

In practice, radiometers are never as simple as those described above and nearly all practical radiometers are *superheterodyne* receivers which incorporate a number of additional steps to produce an output voltage.

The RF front end is the term used to describe all the circuitry between the feed horn and the lower intermediate frequency (IF) stage. The first task of the front end is to amplify the received signal. The radio signals we want to measure are generally very weak and therefore need to be initially amplified by many orders of magnitude so they are above the noise level in succeeding stages. However, the front end electronic components produce random electrical noise which will also get amplified by this large amount. Therefore the role of the pre-amplifier is to amplify the incoming signal from the antenna while adding as little noise as possible. For this reason, the pre-amplifier is often called a low noise amplifier

2.2 Receiving System for an Interferometer

(LNA) and are often cooled to very low temperatures to minimize the amount of noise contributed by the components.

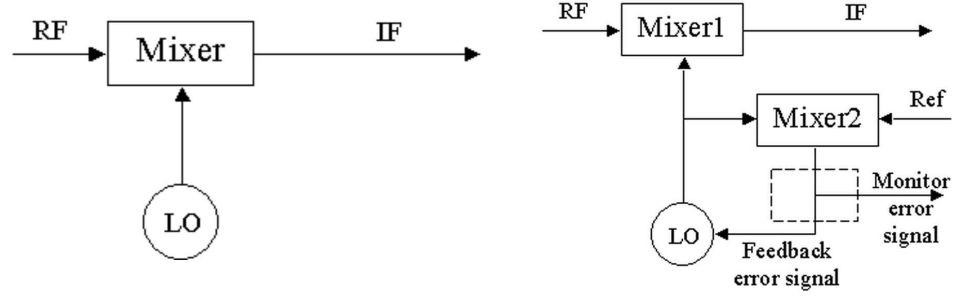


Figure 2.3: *Left:* Block diagram of a simple superheterodyne receiver. The amplified RF signal is mixed with a signal from a local oscillator to convert the signal to the more manageable intermediate frequency. *Right:* For interferometry, a phase lock loop is used to ensure all antennas are locked to the same frequency.

The amplified RF signal is then sent through a mixer which multiplies the RF signal by a sine wave of frequency ν_{LO} which is generated by a local oscillator (LO), as shown in Figure 2.3. The effect of this is that RF signal is changed to a lower frequency which can be easier handled by the IF amplifier and improves frequency selectivity. Mathematically, the mixer does the following

$$2\sin(2\pi\nu_{LO}t) \times \sin(2\pi\nu_{RF}t) = \cos[2\pi(\nu_{LO} - \nu_{RF})t] - \cos[2\pi(\nu_{LO} + \nu_{RF})t], \quad (2.12)$$

and produces two additional outputs, one at the input signal frequency minus the local oscillator frequency, and one at the sum of these frequencies. The lower of the two outputs called the intermediate frequency (IF) is taken by passing the mixer output through a filter in the IF amplifier. In interferometry, where the signals from two antennas are correlated, it is crucial that the receivers from both antennas are operating at the same frequency to control the phase difference between them. This is achieved by using a phase lock system, whose block diagram is laid out in Figure 2.3. In this system another mixer compares the LO to a reference frequency, which is the same for all antennas. Any existing phase error results in an error signal that is sent back to the oscillator so that its frequency can be adjusted to maintain exact frequency tuning. After this, the IF can finally be sent to the radiometer and recorded.

2.3 Fundamentals of Radio Interferometry

The angular resolution $\Delta\theta$ of a radio antenna is the minimum angular separation which two point sources can have in order to be recognized as separate objects. The *Rayleigh criterion* is the generally accepted criterion for defining the angular resolution of a filled circular aperture of diameter D , at the observational wavelength λ and is given as

$$\Delta\theta = 1.22 \frac{\lambda}{D} \text{ rad.} \quad (2.13)$$

The Rayleigh criterion states that two objects are resolved when the first null of the diffraction pattern of one object coincides with the maximum of the diffraction pattern of the other. An immediate consequence of Equation 2.13 is that at large wavelengths, the angular resolution becomes large unless the diameter of the aperture can be increased substantially. In order to achieve modest angular resolution at radio wavelengths with a single radio antenna then, the diameter becomes impractically large. For example, in order to achieve an angular resolution of $1''$ at 6 cm a 12 km aperture would be required. Radio interferometry is a technique used in radio astronomy to overcome this problem of poor angular resolution at long wavelengths.

2.3.1 Young's Slits

The basic principles of interferometry can be understood through Young's double-slit experiment. If coherent radiation emitted from a distant point source propagates through two slits, an illumination pattern composed of bright and dark fringes is observed. The phenomenon is a result of the constructive and destructive interference between the secondary waves produced by the slits. The fringe separation is λ/B , where B is the projected separation of the slits and is called the baseline. The fringe contrast which is historically known as the fringe visibility, V , can be written as

$$|V| = \frac{I_{\max} - I_{\min}}{I_{\max} + I_{\min}} \quad (2.14)$$

where I_{\max} and I_{\min} are the maximum and minimum intensity of the fringes, respectively. In other words, the fringe visibility is the fringe amplitude normalized

by the sum of the maximum and minimum intensity.

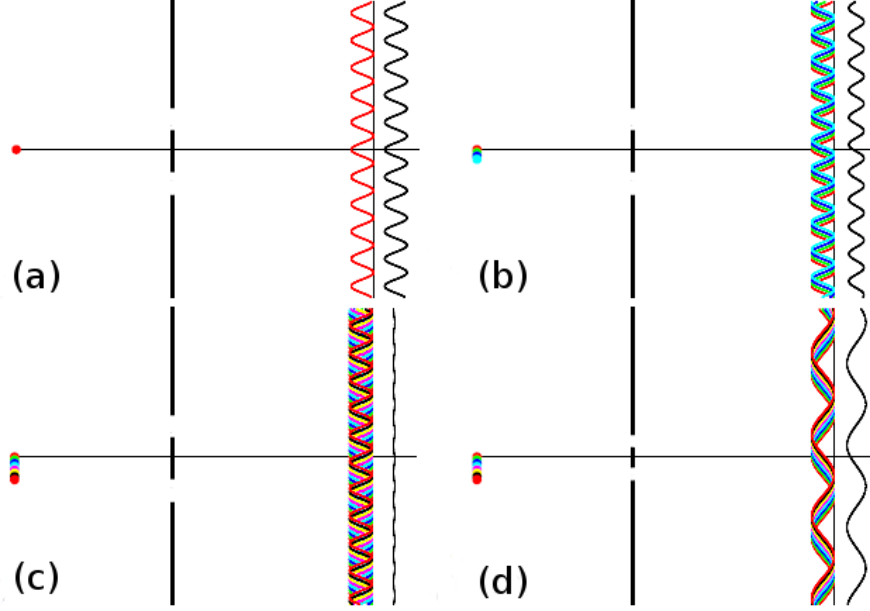


Figure 2.4: The resulting fringe pattern produced by Young’s slits under various conditions. The source is shown on the left of the slits in each panel, while the separate fringe patterns (colors) along with the added fringe pattern (black) is shown on the right of the slits. (a) Point source at infinity, (Visibility = 1). Fringes are separated by an angular distance of λ/B . (b) An increase in source size results in a drop in visibility. (c) When the source size is equal to λ/B , the visibility is zero. (d) If the source size remains the same as in (c) and the slit spacing is reduced, then the fringes re-appear. Figure adapted from [Jackson \(2008\)](#).

In the simple case shown in Figure 2.4a, the angular size of the source is $\ll \lambda/B$ and the fringe visibility is 1. In interferometry, this equates to the situation in which the source size is smaller than the synthesized beam and only an upper limit of the source size can be obtained (i.e., the source is unresolved). In Figure 2.4b, the angular size of the source is now larger and can be thought of as a sequence of point sources each emitting radiation which is uncorrelated with emission from the others. An angular shift of ϕ , called phase, in the sources position results in a shift in the corresponding fringe pattern by the same angle the other way. The total interference intensity pattern is then just the sum of these individual patterns and the visibility is reduced. When the extension of the

2.3 Fundamentals of Radio Interferometry

source equals λ/B , the fringes disappear and give a constant illumination pattern. In this case the fringe visibility is zero and the source is completely resolved as shown in Figure 2.4c. Finally, if the source size is the same as that in Figure 2.4c but the slit separation is reduced, then the fringe separation λ/B will again increase as shown in Figure 2.4d. This is because the source now produces much less displacement of the fringe patterns as a fraction of the fringe separation. In interferometry, this result means that extended sources can only be probed with short baselines.

Visibility and phase are often expressed together as the complex visibility $V = |V|e^{i\phi}$, which completely defines a pattern of interference fringes. Young's double-slit experiment demonstrates a fundamental property of interferometry, namely that the contrast of fringes is a function of the geometry of the source. The results of the experiment are summarized in Figure 2.5. The top row shows that a large source (i.e., one whose intensity distribution extends out to a large angle on the sky) has a fringe visibility pattern which falls off quickly as projected baseline length increases. The bottom row shows that for compact sources the fringe visibility remains high out to large baselines. In the following section we will show that the relationship between the sky brightness distribution $I(\theta)$ and the visibility $V(B)$ is a Fourier transform.

2.3.2 The Two-element Interferometer

Interferometers with N antennas can be treated as $N(N - 1)/2$ independent interferometer pairs so it is worthwhile studying the simplest case of the two-element interferometer. A simplified block diagram of the components of such an interferometer is shown in Figure 2.6. The figure shows two identical antennas separated by a baseline vector \mathbf{b} pointing towards a distant radio source in a direction indicated by the unit vector \mathbf{s} . The plane waves from the distant radio source reach antenna 1 at a time τ_g later than they reach antenna 2. τ_g is called the geometric delay and is given by

$$\tau_g = \frac{\mathbf{b} \cdot \mathbf{s}}{c} = \frac{b \cos \theta}{c} \quad (2.15)$$

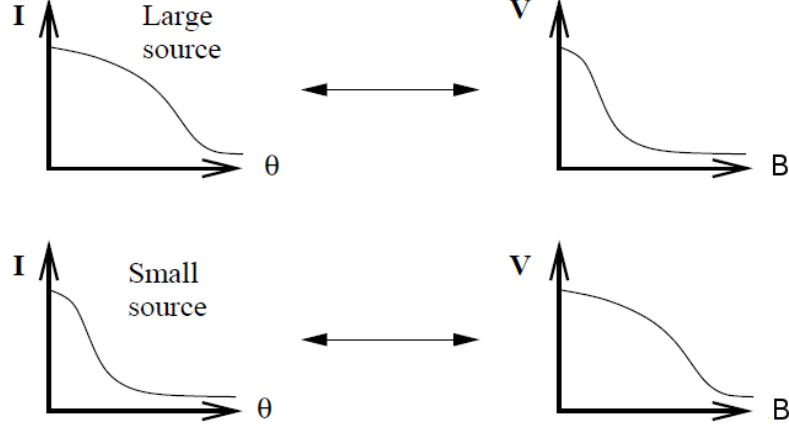


Figure 2.5: *Left column:* Intensity distribution as a function of sky angle for an extended source (top) and for a more compact source (bottom). *Right column:* The corresponding fringe visibility as a function of slit separation or baseline. Figure adapted from [Jackson \(2008\)](#).

where c is the speed of light. If we assume that the interferometer only responds to a very narrow band centered on frequency $\nu = \omega/2\pi$, then the output voltages of antennas 1 and 2 at time t can be written as

$$V_1(t) = V \cos[\omega(t - \tau_g)] \quad \text{and} \quad V_2(t) = V \cos(\omega t). \quad (2.16)$$

The signals are then passed through a correlator which first multiplies these voltages to give

$$V_1(t)V_2(t) = \frac{V^2}{2} [\cos(2\omega t - \omega\tau_g) + \cos(\omega\tau_g)] \quad (2.17)$$

and then averages them over a time interval Δt which is long enough such that $\Delta t \gg (2\omega)^{-1}$ to give the final output R :

$$R = \langle V_1(t)V_2(t) \rangle = \frac{V^2}{2} [\cos(\omega\tau_g)]. \quad (2.18)$$

As the Earth rotates, τ_g varies slowly with time and the resultant oscillations in the correlator output voltage represent the motion of the source. These

2.3 Fundamentals of Radio Interferometry

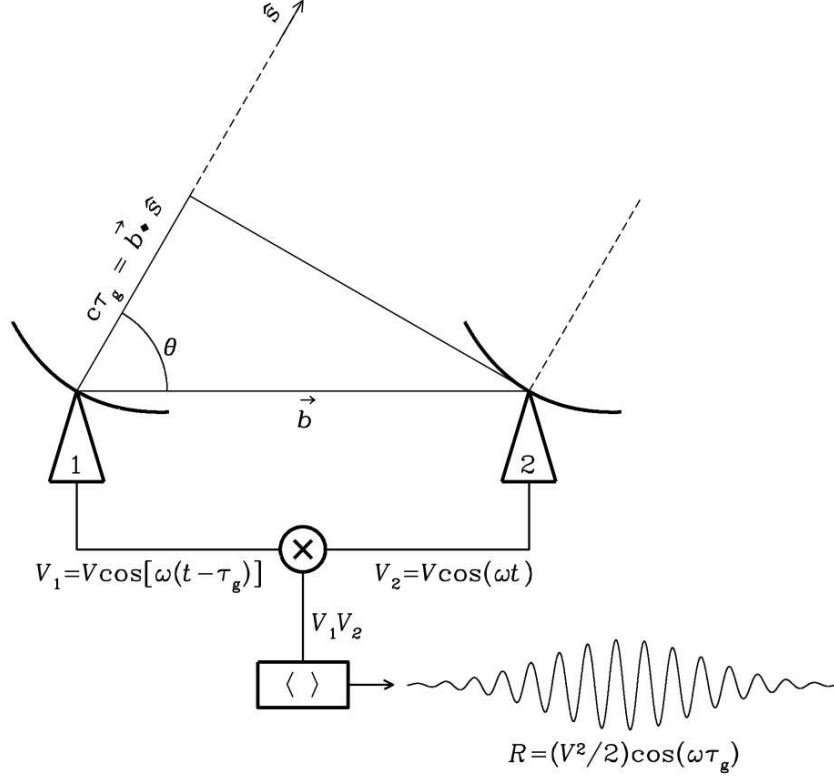


Figure 2.6: Simplified schematic diagram of a two-element interferometer. The correlator multiplies and averages the voltage outputs V_1 and V_2 of the two dishes and yields an output amplitude $V^2/2$ which is proportional to the point-source flux density F_ν . *Image Credit:* National Radio Astronomy Observatory.

sinusoidal oscillations are called fringes, and the fringe phase is

$$\phi = \omega \tau_g = \frac{\omega b \cos \theta}{c} \quad (2.19)$$

which changes with source direction as follows

$$\frac{d\phi}{d\theta} = \frac{\omega b \sin \theta}{c} = 2\pi \left(\frac{b \sin \theta}{\lambda} \right). \quad (2.20)$$

The fringe phase completes a full period (i.e., $\Delta\phi = 2\pi$) when an angular change $\Delta\theta = (\lambda/b \sin \theta)$ occurs. This tells us that the fringe phase is an extremely sensitive measure of source position if the projected baseline $b \sin \theta$ is many wavelengths long

2.3 Fundamentals of Radio Interferometry

and is the reason why interferometers can determine the positions of compact radio sources with exquisite accuracy.

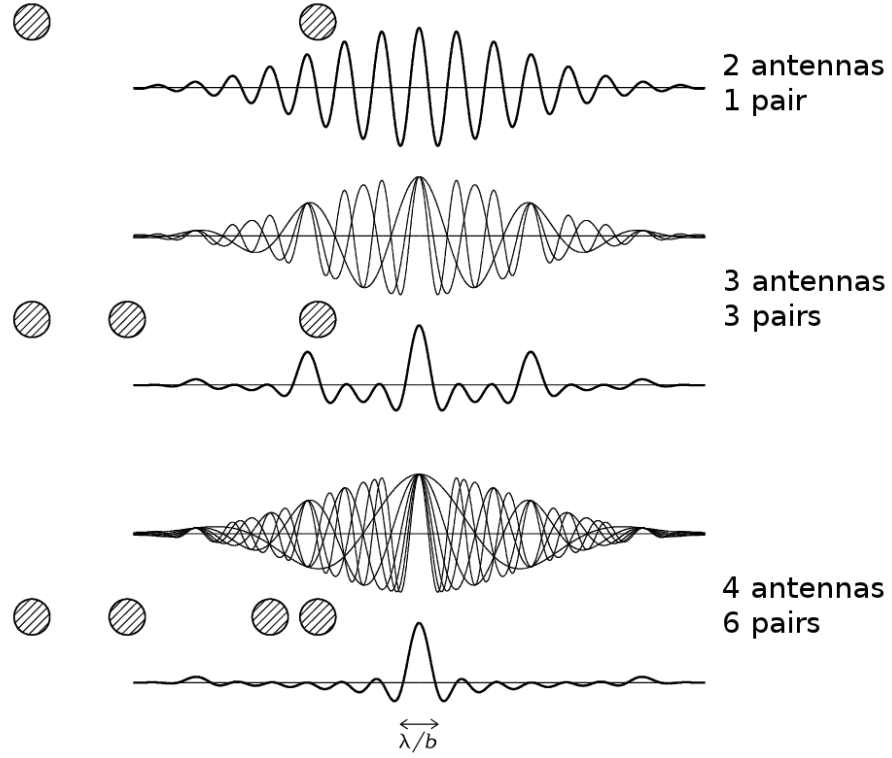


Figure 2.7: The instantaneous point source responses of an interferometer with two, three and four elements is indicated by the thick curves. The individual responses of the three pairs of two-element interferometers of the three-element interferometer and the six pairs of two-element interferometers of the four-element interferometer are plotted as thin curves. The main beam of the four-element interferometer is nearly Gaussian and has a width of $\sim \lambda/B$. This is known as the instantaneous synthesized beam of the interferometer. *Image Credit:* National Radio Astronomy Observatory.

If the antennas in an interferometric array are isotropic, then the point-source response of the interferometer would be a sinusoid spanning the entire sky and the interferometer would be only sensitive to one Fourier component of the sky brightness distribution having angular period $\lambda/b\sin\theta$. The response of a two-element interferometer R with non-isotropic antennas is this sinusoid multiplied by the product of the voltage patterns (i.e., defined as $f(u, v)$ in Section 2.1.1)

2.3 Fundamentals of Radio Interferometry

of the individual antennas. If the antennas are identical then this product is the power pattern of the individual antennas called the primary beam. The primary beam is usually a Gaussian that is much wider than the fringe period as $D \ll b \sin \theta$. The result is that an interferometer with directive antennas responds to a finite range of angular frequencies centered on $b \sin \theta / \lambda$. The instantaneous point source response of an interferometer is known as the synthesized beam and is the point source response obtained by averaging the outputs of all antenna pairs. The synthesized beam of an interferometer is an important quantity as it defines the maximum angular resolution of the instrument. The synthesized beams produced by an interferometer with a various number of antennas arranged in 1-D is shown in Figure 2.7. The figure shows that the synthesized beam can be improved by acquiring more Fourier components (i.e., baselines) and rapidly approaches a Gaussian as N increases. However, sidelobes are still significant and a broad negative “bowl” exists between the main beam and the first sidelobes due to the absence of short spacings.

2.3.3 Complex Visibility

The interferometer output can be expressed in terms of the radio brightness over the sky, which is sometimes also called specific intensity and has units $\text{W m}^{-2} \text{Hz}^{-1} \text{sr}^{-1}$. If the radio brightness of a spatially incoherent extended source in the direction of unit vector \mathbf{s} is $I(\mathbf{s})$, then the response of the two-element interferometer with “cosine” correlator output near frequency $\nu = \omega/2\pi$ is obtained by treating the extended source as the sum of independent point sources:

$$R_c = \int_{\Omega} \mathcal{A}(\mathbf{s}) I_{\nu}(\mathbf{s}) \cos \left(\frac{2\pi \mathbf{b} \cdot \mathbf{s}}{\lambda} \right) d\Omega \quad (2.21)$$

where \mathcal{A} is the normalized antenna reception pattern defined in Section 2.1.1 and we call $\mathcal{A}(\mathbf{s}) I_{\nu}(\mathbf{s})$ the modified brightness distribution. However, the cosine function in the “cosine” correlator output is only sensitive to the even part of the sky brightness distribution, which can be written as the sum of even and odd parts:

$$I(\mathbf{s}) = I_e(\mathbf{s}) + I_o(\mathbf{s}). \quad (2.22)$$

2.3 Fundamentals of Radio Interferometry

A “sine” correlator whose output is odd, is needed to detect the odd part of $I(\mathbf{s})$ and this is implemented by inserting a 90° phase delay into the signal of one of the antennas to give

$$R_s = \int_{\Omega} \mathcal{A}(\mathbf{s}) I_{\nu}(\mathbf{s}) \sin\left(\frac{2\pi \mathbf{b} \cdot \mathbf{s}}{\lambda}\right) d\Omega \quad (2.23)$$

It is convenient to write the cosines and sines as complex exponentials using the identity

$$e^{i\phi} = \cos(\phi) + i\sin(\phi) \quad (2.24)$$

and so the combination of “cosine” and “sine” correlators is called a “complex” correlator. The term *visibility* was first introduced by [Michelson \(1890\)](#) to describe the relative amplitudes of the optical fringes that he observed. The visibility is a complex quantity in radio astronomy and has dimensions of spectral power flux density ($\text{W m}^{-2} \text{Hz}^{-1}$). The complex visibility is the response of a two-element interferometer with a complex correlator to an extended source with brightness distribution $I(\mathbf{s})$ and is defined as

$$V \equiv R_c - iR_s, \quad (2.25)$$

i.e.,

$$V_{\nu} = \int_{\Omega} \mathcal{A}(\mathbf{s}) I_{\nu}(\mathbf{s}) e^{-2\pi i \nu \mathbf{b} \cdot \mathbf{s} / c} d\Omega. \quad (2.26)$$

2.3.4 Coordinate Systems for Imaging

The baseline vector \mathbf{b} has coordinates (u, v, w) in three dimensions shown in Figure 2.8 where w points in the directions of interest, i.e., towards a direction s_0 that becomes the center of the synthesized image. u , v and w are measured in wavelengths (i.e., the components of \mathbf{b}/λ) and have directions towards the East, the North and the phase tracking center, respectively. An arbitrary unit vector \mathbf{s} has components (l, m, n) called direction cosines, where $n = \cos\theta =$

$(1 - l^2 - m^2)^{1/2}$. Using these coordinates the parameters in Equation 2.26 become

$$\begin{aligned} \frac{\nu \mathbf{b} \cdot \mathbf{s}}{c} &= ul + vm + wn, \\ d\Omega &= \frac{dl dm}{n} = \frac{dl dm}{\sqrt{1 - l^2 - m^2}}. \end{aligned} \quad (2.27)$$

Therefore Equation 2.26 can be defined in terms of the coordinate system laid out in Figure 2.8 as

$$V_\nu(u, v, w) = \int_{-\infty}^{\infty} \int_{-\infty}^{\infty} \mathcal{A}_\nu(l, m) I_\nu(l, m) e^{-2\pi i [ul + vm + w(\sqrt{1 - l^2 - m^2})]} \frac{dl dm}{\sqrt{1 - l^2 - m^2}} \quad (2.28)$$

which is not a three-dimensional Fourier transform. This equation becomes a two-dimensional Fourier transform if $w = 0$ which is a good approximation for small field imaging, i.e., when $|l|$ and $|m|$ are small. In this case Equation 2.28 can be inverted to find the modified sky brightness distribution:

$$\mathcal{A}_\nu(l, m) I_\nu(l, m) = \int_{-\infty}^{\infty} \int_{-\infty}^{\infty} V_\nu(u, v) e^{2\pi i (ul + vm)} du dv. \quad (2.29)$$

Therefore Equation 2.29 demonstrates the important Fourier Transform relationship between the sky brightness distribution and the complex visibility (i.e., the interferometer response).

2.4 Synthesis Imaging

A synthesis imaging telescope consists of a number radio antennas fixed on the ground and uses the Earth's rotation to vary the projected baseline coverage to increase the sampling of the $u - v$ plane. In this section we describe how Earth-rotation aperture synthesis is used to convert the complex visibilities outputted from the correlator to a final radio image of the observed sky.

2.4.1 Visibility Sampling

An example of how a radio interferometer samples the $u - v$ plane is shown in Figure 2.9. The left panel of this figure shows the overhead view of the VLA in its

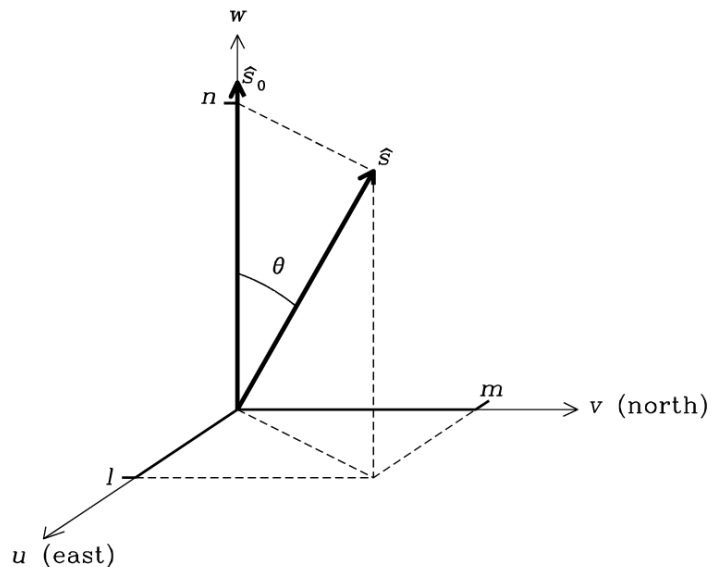


Figure 2.8: The (u, v, w) interferometric coordinate system. l , m , and n are the projections of the unit vector \mathbf{s} onto the u , v , and w axes, respectively.

most extended configuration while the other two panels shows the corresponding $u-v$ coverage for different periods of time. We define u and v as the east-west and north-south components of the projected baseline in wavelengths, respectively. As the Earth rotates, the projected baseline of every two-element pair in the array changes, thus sampling a different part of the $u-v$ plane. The middle panel shows that the total $u-v$ coverage of the VLA for a very short duration track (i.e., a snapshot) results in a ‘snowflake’ like pattern, with more dense coverage in the direction of the arms of the array due to the larger number of baselines. Most radio interferometers have their own unique array configuration layout and thus produce a different ‘snapshot’ $u-v$ coverage to that shown in Figure 2.9. Over many hours, the $u-v$ points trace out portions of ellipses and eventually after a full Earth rotation the points can trace out full ellipses as shown in the right panel of Figure 2.9.

2.4.2 Imaging (Making a Dirty Map)

For every sky brightness distribution $I(l, m)$ there exists a continuous complex visibility function $V(u, v)$ that is its Fourier Transform. An array of antennas

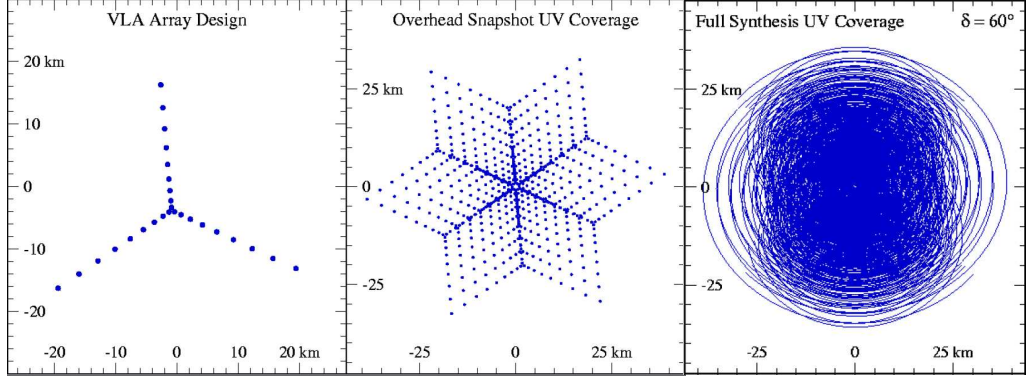


Figure 2.9: *Left:* The VLA in A-configuration is an example of an ‘Y’ shaped array design. *Middle:* The corresponding overhead snapshot $u-v$ coverage results in ‘snowflake’ pattern. *Right:* The corresponding $u-v$ coverage after a 12 hour track of a source at a declination of 60° . Note the more intense $u-v$ coverage in the direction of the three straight arms of the VLA for a snapshot track compared to the more uniform coverage over a longer duration track.

will only ever measure a certain set of values of this visibility function where the measured set is called the sampling function $S(u, v)$. This function is zero where no data have been taken. The actual data provided by the array is known as the sampled visibility function, $S(u, v)V(u, v)$. If we take the inverse Fourier transform of this function we get what is known as the *dirty image*:

$$I_\nu^D(l, m) = \int_{-\infty}^{\infty} \int_{-\infty}^{\infty} S(u, v) V_\nu(u, v) e^{2\pi i(ul+vm)} du dv. \quad (2.30)$$

where we have used $I_\nu(l, m)$ to denote the modified sky brightness $\mathcal{A}(l, m)I_\nu(l, m)$ as the correction for primary beam can be made at the final stage of data processing. Using the convolution theorem, the relationship between the dirty image and the desired intensity distribution $I_\nu(u, v)$ is

$$I_\nu^D(u, v) = I_\nu(u, v) * B(l, m) \quad (2.31)$$

where the asterisk implies convolution and

$$B(l, m) = \int_{-\infty}^{\infty} \int_{-\infty}^{\infty} S(u, v) e^{2\pi i(ul+vm)} du dv \quad (2.32)$$

is the *point spread function* (PSF), or *synthesized beam*, or *dirty beam* (i.e., the inverse Fourier Transform of the sampling function S). Equation 2.31 says that the dirty image I^D is the true intensity distribution I , convolved with the synthesized beam B .

In Figure 2.10 we graphically summarize what has been said above. The panels in the upper row show the sky plane representations of the true image, the point spread function and the dirty image, while the panels in the lower row show the corresponding $u-v$ plane representations of the true visibility, the sampling function and the sampled visibility. In other words, Equation 2.29 is summarized graphically by the relationship between panels (a) and (d), Equation 2.32 by (b) and (e), and Equations 2.30 and 2.31 by (c) and (f).

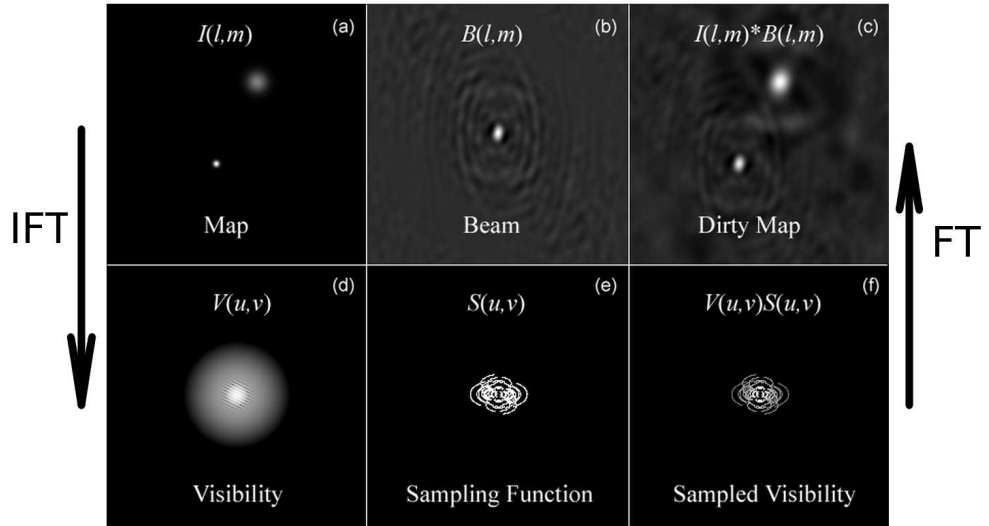


Figure 2.10: The Fourier transform pairs in synthesis imaging. (a) and (d): The true sky brightness and the visibility. (b) and (e): The dirty beam and the sampling function. (c) and (f): The dirty image and the sampled visibility. *Image Credit:* Prof. Dale E. Gary (New Jersey Institute of Technology).

Before the dirty image is computed, a weighting system is often applied to the visibilities to control the PSF. The two most common types of weighting system used are:

$$D_k = 1, \quad \text{natural weighting} \quad (2.33)$$

$$D_k = \frac{1}{N_s(k)}, \quad \text{uniform weighting} \quad (2.34)$$

where D_k is the weight to be applied to cell k , and $N_s(k)$ is the number of data samples falling into cell k of characteristic width s . Natural weighting treats all points alike and gives the best signal-to-noise ratio for detecting weak sources. However, it produces a beam with a broad low-level plateau which is undesirable when imaging sources with both large and small scale structure. Uniform gridding produces fewer artifacts in the final map, while keeping the full resolution of the array but gives poorer signal-to-noise than natural weighting.

The ‘direct Fourier transform’ method can then be used to solve for the dirty image Equation 2.30. However, if this method is evaluated at every point on a $N \times N$ grid, then the number of multiplications required goes as N^4 . The fast Fourier transform (FFT) algorithm can also be used to solve Equation 2.30 but requires interpolating the data onto a regular grid (i.e., a process known as *gridding*). This method is widely used for large data volumes as it requires only a few times $N^2 \log_2 N$ operations - not $\mathcal{O}(N^4)$, and the total time taken for gridding and FFT is usually a lot less than would take using the direct Fourier transform method.

2.4.3 Deconvolution (Making a CLEAN map)

The solution to the inverse Fourier transform given in Equation 2.29 is not unique, because the unmeasured points in the $u - v$ plane could have *any* value without violating the data constraints. The ‘principle solution’ is the one in which all missing $u - v$ measurements are set to zero and gives the dirty image discussed in the previous section. The dirty image is usually not a satisfactory representation of the sky as one would expect a more continuous distribution of visibilities than that provided by the array. The goal of the deconvolution process is to find a method that determines more reasonable values for the unmeasured $u - v$ data. A priori information is the key to choosing ‘reasonable’ values. For example, we know that the Stokes parameter I must be positive and that radio sources generally do not have sidelobe patterns.

The CLEAN algorithm (Högbom, 1974) is the most widely used technique in radio interferometry to deconvolve the true sky intensity from the dirty beam. It assumes that the radio source can be represented by a number of point sources in an otherwise empty field and a simple iterative process is used to find the strengths and positions of these point sources. The final CLEAN image (i.e., the deconvolved image) is the sum of these point sources convolved with a CLEAN beam, which is usually an elliptical Gaussian of the same size and shape as the inner part of the dirty beam. The CLEAN algorithm obeys the following steps:

1. Find the strength and position of the brightest point in the dirty image. It may also be desirable to search for peaks in specified areas of the image, called CLEAN windows or regions.
2. At this position in the dirty image, subtract the dirty beam multiplied by the peak strength and a damping factor g ($g \leq 1$, usually called the loop gain).
3. Record the position and the subtracted flux in a model.
4. Iterate between (1), (2), and (3) until the peak is below some user specified level. The remainder of the dirty image is now termed the residuals.
5. Convolve the accumulated point source model with an idealized CLEAN beam (usually an elliptical gaussian of the same size and shape as the central lobe of the dirty beam).
6. Add the residuals to the image in (5) to create the final CLEAN image.

A problem with CLEAN is that the final CLEANed image is somewhat dependent upon the various control parameters such as CLEAN boxes, the loop gain and the number of CLEAN subtractions. For example, using too high a gain tends to make extended, weak emission undetectable and noisy. This problem is unavoidable, and input values must be chosen on a case by case basis, depending on the source and data quality.

Another deconvolution algorithm used in radio synthesis imaging, albeit less often, is the Maximum Entropy Method (MEM) which operates by minimizing a

smoothness function (‘entropy’) in an image. To conclude this section, we briefly discuss the practical differences between CLEAN and MEM:

1. CLEAN is nearly always faster than MEM, unless the image contains more than 1 million pixels.
2. MEM images are nearly always smoother than CLEAN images. This is because for CLEAN, what happens at one pixel is not coupled to what happens to its neighbours, while MEM couples pixels together by minimizing the spread in pixel values.
3. CLEAN sometimes makes extended emission look blotchy and may introduce artificial stripes into the image while MEM copes very poorly with point sources in extended emission. (Multi-scale CLEAN which is discussed in Chapter 3 is now becoming a popular choice in the radio community as an alternative deconvolution algorithm for images containing extended emission.)
4. For MEM, it is necessary to know the noise level quite well and it also helps to know the total flux density of the image. Knowledge of these are not required for CLEAN.

3

Targets, Instrumentation, and Observations

3.1 Betelgeuse

decin proposal, paper intro, CO

3.2 CARMA

3.3 CARMA Observations of Betelgeuse

3 configurations, max and min resolutions, variability of phase cals, flux cals

3.3 CARMA Observations of Betelgeuse

Table 3.1: Physical Properties of α Ori.

Property	α Ori	Reference
HD Number	124897	
Spectral Type	K2 III	
ra (ICRS: ep=J2000)	14 ^h 15 ^m 39.672 ^s	
dec (ICRS: ep=J2000)	+19 10 56.673	
pm-ra (mas yr ⁻¹)	-1093.39 \pm 0.44	
pm-dec (mas yr ⁻¹)	-2000.06 \pm 0.39	
π (mas)	88.83 \pm 0.54	
Distance (pc)	11.3 \pm 0.1	
M (M_{\odot})	0.8 \pm 0.2	
θ_{UD} (mas)	21.0 \pm 0.2	
θ_{LD} (mas)	21.0 \pm 0.2	
L (L_{\odot})		
R (R_{\odot})	25.4 \pm 0.3	
Log g		
T_{eff} (K)	4294 \pm 30	
v_{rad} (km s ⁻¹)	+5.19 \pm 0.04	
v_{esc} (km s ⁻¹)	110	
v_{∞} (km s ⁻¹)	\sim 40	
T_{wind} (K)	\sim 10,000	
\dot{M} (M_{\odot} yr ⁻¹)		
H (H_{\odot})		
Fe/H	-0.5 \pm 0.2	

Table 3.2: CARMA Observations of α Ori between June 2007 and November 2009.

Date	Configuration	Time on Source (hr)	Flux Calibrator	Phase Calibrator	Image Cube Dynamic Range
2007 Jun 18	D	0.9	0530+135	0530+135, 0532+075	22.8
2007 Jun 21	D	3.0	0530+135	0530+135, 0532+075	22.7
2007 Jun 24	D	2.1	0530+135	0530+135, 0532+075	26.1
2007 Jun 25	D	2.4	0530+135	0530+135, 0532+075	30.2
2009 Jul 07	E	3.2	3C120	3C120, 0532+075	30.1
2009 Nov 05	C	1.2	3C120	3C120, 0532+075	17.3
2009 Nov 09	C	3.0	3C120	3C120, 0532+075	27.2
2009 Nov 15	C	1.0	3C120	3C120, 0532+075	17.8
2009 Nov 16	C	3.2	3C120	3C120, 0532+075	32.0
All	C	8.4	43.8
All	D	8.4	31.9
All	Multi-configuration	20.0	52.3

3.4 Arcturus and Aldebaran

Currently the most detailed spatial information about the atmospheres of K and early M evolved stars is obtained from eclipsing binaries such as the ζ Aurigae and symbiotic systems (e.g., [Wright 1970](#); [Baade *et al.* 1996](#); [Eaton 2008](#); [Crowley *et al.* 2008](#)). Even though these systems offer us the best opportunity to obtain information on the dynamics and thermodynamics at various heights in the evolved star’s atmosphere, the very nature of the binary system may introduce further complexities. For example, the orbital separation is often within the wind acceleration region and one could expect flow perturbations to be present (e.g., [Chapman 1981](#)). In fact, using the old VLA, [Harper *et al.* \(2005\)](#) were able to confirm that the velocity structure of ζ Aurigae is not typical of single stars with similar spectral types, such as λ Velorum ([Carpenter *et al.*, 1999](#)). In order to avoid the assumed additional complexities of a companion, we have selected two single luminosity class III red giants: Arcturus (α Boo: K2 III) and Aldebaren (α Tau: K5 III). These nearby red giants have been extensively studied at other wavelengths and their stellar parameters, which are summarized in Table 3.3, are accurately known. These stars are predicted to be point sources at all frequencies between 1 and 50 GHz in all VLA configurations so our radio observations measure their total flux density, F_ν . For example, our observations of these stars which are discussed in Section 3.6, were taken in B configuration providing a maximum angular resolution of $\sim 0.14''$ at 45 GHz which is equivalent to $\sim 7 R_\star$ for both stars. The radio emission from these stars at 45 GHz is expected to be chromospheric in origin ([Harper *et al.*, 2013](#)), and as the spatial extent of red giant chromospheres is expected to be less than $1.5 R_\star$ ([Berio *et al.*, 2011](#)), then we can be assured that these targets will be unresolved even at the highest VLA frequencies. Moreover, both stars have existing semi-empirical 1-D chromospheric and wind models which we directly compare to our data.

Arcturus (α Boo: K2 III)

Arcturus (α Boo: K2 III) is the nearest ($d = 11.3$ pc) and brightest ($V = -0.04$ mag) noncoronal red giant and is probably the best example of a red giant whose atmosphere can be studied in detail with the VLA. It is the leader of a group

of stars that share a similar V space velocity (the component of stellar motion relative to the LSR in the direction of rotation), age (≥ 10 Gyr), and metallicity ($[\text{Fe}/\text{H}] \sim -0.5$), known as the Arcturus moving group (Eggen, 1971). The group has traditionally been regarded as the remains of a dissolved open cluster (e.g., Eggen, 1971, 1996) but it has also been suggested to be the debris of a metal-poor accreted satellite some billions of years ago (Navarro *et al.*, 2004). Recent analysis of chemical abundances are consistent with the former hypothesis but do not entirely rule out a merger one (Williams *et al.*, 2009). Arcturus is ascending the red giant branch and being a single star, its mass is relatively poorly constrained but is similar to that of the Sun ($0.8 \pm 0.2 M_{\odot}$ by Kallinger *et al.*, 2010). During the last decade there has been a large dispersion in the reported values of Arcturus' effective temperature (a nice graph summarizing this is presented in Griffin, 1996) but nowadays it is generally accepted to be about 4300 K (di Benedetto, 1993). A number of interferometric measurements of the limb-darkened angular diameter of the star are available in the literature with most values agreeing within their uncertainties. The weighted mean value of these values is $\theta_{\text{LD}} = 21.06 \pm 0.17$ mas (Ramírez & Allende Prieto, 2011) giving the star a radius of $25.4 \pm 0.3 R_{\odot}$.

Arcturus is an important target for high spatial and spectral resolution calibration. Thus when the Hipparcos catalogue flagged Arcturus as a two component object (Perryman *et al.*, 1997) it caused quite a stir in the community. However, the uncertainties in the Hipparcos data (Soderhjelm & Mignard, 1998) along with a non-detection in adaptive optics observations (Turner *et al.*, 1999) and sensitive interferometric techniques (Lacour *et al.*, 2008) suggest that Arcturus is single and can still be used as a calibrator. Nevertheless, Lacour *et al.* (2008) still do not rule out the possibility of a planetary companion of a few Jovian masses as suggested by its long period radial velocity variations of $\sim x$ days (Brown, 2007; Hatzes & Cochran, 1993). Variations in the order of a few days period are also seen in its radial velocity (Merline, 1999) as well as photometry (Retter *et al.*, 2003). The photometric amplitude oscillations can vary by up to a percent and may be the manifestation of convection such as large-scale granulation, or solar-like oscillations (Dziembowski *et al.*, 2001).

The first detailed model of the atmosphere of Arcturus was the 1-D time-independent semi-empirical model of Ayres & Linsky (1975) which was based

3.4 Arcturus and Aldebaran

on diagnostics observable from the ground (i.e. Ca II *h* and *k* and the Ca II IR triplet) and early satellite observations of the Mg II *h* and *k* emission lines from

Table 3.3: Basic Properties of α Boo and α Tau.

Property	α Boo	α Tau	Reference
HD Number	124897	29139	...
Spectral Type	K2 III	K5 III	1
App. Mag. (V)	-0.5	0.86v	1
ra (ICRS: ep=J2000)	14 ^h 15 ^m 39.672 ^s	04 ^h 35 ^m 55.239 ^s	3
dec (ICRS: ep=J2000)	+19 10 56.673	+16 30 33.489	3
pm-ra (mas yr ⁻¹)	-1093.39 ± 0.44	63.45 ± 0.84	3
pm-dec (mas yr ⁻¹)	-2000.06 ± 0.39	-188.94 ± 0.65	3
π (mas)	88.83 ± 0.54	48.94 ± 0.77	3
Distance (pc)	11.3±0.1	20.4±0.3	3
M (M_{\odot})	0.8±0.2	1.3±0.3	6, 4
θ_{LD} (mas)	21.06±0.17	20.58±0.03	5a, 5b
R (R_{\odot})	25.4±0.3	44.2±0.9	...
T_{eff} (K)	4294±30	3970±49	5
L (L_{\odot})	calc	calc	...
Log g	calc	calc	...
v_{rad} (km s ⁻¹)	+5.19 ± 0.04	+54.11 ± 0.04	9
v_{esc} (km s ⁻¹)	110	106	...
v_{∞} (km s ⁻¹)	35 – 40	30	7, 8
T_{wind} (K)	~10,000	~10,000	7, 8
\dot{M} (M_{\odot} yr ⁻¹)	2×10^{-10}	1.6×10^{-11}	7, 8
H (H_{\odot})	calc	calc	...
Fe/H	-0.5 ± 0.2	-0.15 ± 0.2	10
Rotational period (yr)	2.0 ± 0.2	1.8	11, 12
B (G)	0.65 ± 0.26	?	13
Chromosphere Model	Drake (1985)	McMurry (1999)	...
Wind Model	Drake (1985)	Robinson <i>et al.</i> (1998)	...

References.-(1)Perryman *et al.* (1997); (2)Gray *et al.* (2006); (3)van Leeuwen (2007); (5a) Ramírez & Allende Prieto (2011) (5b) Richichi & Roccatagliata (2005); (5)di Benedetto (1993); (6)Kallinger *et al.* (2010); (7)Drake (1985); (8)Robinson *et al.* (1998); (9)Massarotti *et al.* (2008); (10)Decin *et al.* (2003); (11) Gray *et al.* (2006); (12) Hatzes & Cochran (1993); (13) (Sennhauser & Berdyugina, 2011)

Copernicus. They were able to calculate temperature and mass column densities for the upper photosphere and chromosphere and estimated the temperature at the top of the chromosphere to be ~ 8000 K. They also found that $T_{\min}/T_{\text{eff}} \sim 0.77$ which is similar to that of the Sun. The important IUE cool star survey by [Linsky & Haisch \(1979\)](#) placed Arcturus on the right of the dividing line. This meant that its atmosphere showed lines formed at temperatures no hotter than $10,000 - 20,000$ K, suggestive of a chromosphere only. However, they also developed a hot coronal wind model for the star and found it to be consistent with the absence of transition region material in the IUE data; that is, the high temperature transition region emission line fluxes could be below the detection limit. [Drake \(1985\)](#) developed a semi-empirical chromosphere and wind model for Arcturus based on the Mg II *k* emission line from IUE and showed that its wind is very extended and estimated a mass loss rate of $2 \times 10^{-10} M_{\odot} \text{ yr}^{-1}$. Evidence began to emerge that Arcturus actually falls into the class of late type stars known as hybrids when deeply exposed IUE echelle spectrograms showed the weak presence of the Si III] $\lambda 1892.0$ feature, indicating the existence of a small amount of plasma at temperatures as hot as 6×10^4 K. Its hybrid status was confirmed when C IV and N V (indicative of temperatures $\sim 1 \times 10^5$ K) were detected with the HST STIS and also with a tentative 3σ X-ray detection made with the Chandra X-Ray Observatory ([Ayres et al., 2003](#)). The important conclusion is that Arcturus has been able to sustain a modest level of magnetic activity. In fact, a magnetic field (albeit weak) has recently been directly detected on the star via the Zeeman effect ([Sennhauser & Berdyugina, 2011](#)), and a magnetic cycle with a period of ≥ 14 years has also been reported ([Brown et al., 2008](#)).

Arcturus appears to have a thermally bifurcated chromosphere which consists of material within the chromosphere that is cooler than the surrounding chromospheric temperature minimum [i.e a CO-mosphere, [Wiedemann et al. \(1994\)](#)]. This suggests that the assumption in current semi-empirical chromospheric models of the *hot* UV emitting material having a filling factor of unity may not be exactly correct. The more recent spectroscopic analysis of CO and H₂O transitions have confirmed the existence of cooler molecular *clouds* in the outer atmosphere of Arcturus ([Ryde et al., 2002](#); [Tsuji, 2009](#)). We defer the discussion of all previous radio measurements of the star until Chapter 6.

Aldebaran (α Tau: K5 III)

At a distance of 20.4 pc, Aldebaran (α Tau: K5 III) is a nearby red giant and is one of the most easily recognizable stars from the northern and most of the southern hemisphere. Even though it is almost twice as far away as Arcturus, its large stellar radius ($R_{\star} = 44.2 \pm 0.9 R_{\odot}$) gives it a comparable angular diameter ($\theta_{\text{LD}} = 20.58 \pm 0.03$), and is therefore another good candidate for multi-frequency studies with the VLA. Its effective temperature ($T_{\text{eff}} = 3970 \pm 49$ K) is slightly lower than Arcturus', and also has a slightly higher mass ($M = 1.3 \pm 0.3 M_{\odot}$). Combining this mass and with a radius of $x R_{\odot}$ results in a surface gravity of $\log g = x$ (in units of cm s^{-2}), x times lower than that of the Sun. The metallicity of Aldebaran is marginally subsolar with $[\text{Fe}/\text{H}] = -0.15 \pm 0.2$ (Decin *et al.*, 2003). Using high spectral resolution in the H, K, and L bands, Tsuji (2008) derived the carbon, nitrogen, and oxygen abundances in Aldebaran which suggests the mixing of the CN-cycled material in the first dredge-up. A 643 day period in the radial velocity for Aldebaran was reported by Hatzes & Cochran (1993) and Hatzes & Cochran (1998) find evidence to support the hypothesis that this variability comes from the reflex motion of the central star due to a planetary companion having a mass of $11 M_{\text{Jup}}$.

Aldebaran has been extensively studied at UV wavelengths. Early IUE observations placed the star well to the noncoronal side of the Linsky-Haisch dividing line (Linsky & Haisch, 1979). The first chromospheric model of the star was developed in the late 1970s (Kelch *et al.*, 1978) and was based on both optical (mainly Ca II H and K) and UV (Mg II h and k) emission line fluxes. Later, GHRS spectra revealed the presence of significant flux in the C IV resonance lines around 1550 Å (Carpenter & Robinson, 1996), indicating the presence of *hot* transition region plasma. In light of the new GHRS findings, a new model of the chromosphere and transition region of Aldebaran was developed, with temperatures reaching up to $T_e \sim 1 \times 10^5$ K. Modelling the GHRS optically thick Mg II and O I resonance lines (which show the most evidence for the stellar wind), Robinson *et al.* (1998) found evidence for the acceleration of a slow wind and derived a mass-loss rate of $1.6 \times 10^{-11} M_{\odot} \text{ yr}^{-1}$, and a terminal wind velocity of 30 km s^{-1} . Unexpectedly, FUSE spectra revealed the presence (albeit

3.5 The Karl G. Jansky Very Large Array

weak) of the coronal proxy O VI 1032 and 1038 Å emission lines (Dupree *et al.*, 2005) although Ayres *et al.* (2003) failed to detect any X-ray emission from the star.

Wiedemann *et al.* (1994) observed Aldebaran’s infrared ro-vibration absorption lines ($v = 2 - 1$) and matched them with synthetic spectra based on a model containing the semi-empirical photosphere of Kelch *et al.* (1978) and the best fitting temperature and column density profiles. Like Arcturus, they found a steady decrease in temperature with height, with the chromospheric temperature being constantly below the temperature minimum ($T_e^{\min} \sim 2800$ K) of the Kelch model. Like Arcturus, they explained their results by suggesting the existence of an extra *cool* component in the outer atmosphere (i.e. a thermally bifurcated CO-mosphere). Recently, Ohnaka observed the CO first overtone lines ($v = 2 - 0$) of Arcturus near $2.3 \mu\text{m}$ with the Very Large Telescope Interferometer (VLTI) and discovered a CO layer extending out to $2.5 R_\star \pm 0.3 R_\star$. They were unable to constrain the geometrical thickness of this CO layer from their data but we will show how our VLA radio data can constrain this value in Chapter 6. H₂O was also confined in its MOLsphere when Tsuji (2001) detected a H₂O absorption feature at $\sim 6.6 \mu\text{m}$. A narrow absorption feature in the midst of the wind absorption of the GHRS Mg II h and k lines has been interpreted and modelled as a feature of α Tau’s wind-ISM interaction region also known as its astrosphere (Wood *et al.*, 2007). Finally, there has been a few sporadic radio continuum measurements of Aldebaran and these will be discussed in detail in Chapter 6.

3.5 The Karl G. Jansky Very Large Array

The Karl G. Jansky Very Large Array (VLA) is an aperture synthesis radio telescope located on the Plains of San Agustin, New Mexico, USA and is capable of producing radio images with a resolution comparable to that of optical telescopes. It is the product of a program to modernize the electronics of the old VLA which had been in operation since the late 1970’s. One of the main upgrades to the VLA is the addition of the Wideband Interferometric Digital Architecture (WIDAR) correlator which allows the digital correlation of very wideband signals. WIDAR digitally filters and splits the data into sub-bands which are then

3.5 The Karl G. Jansky Very Large Array

Table 3.4: Improved Performance Parameters of the VLA.

Parameter	old VLA	VLA	Improvement Factor
Continuum sensitivity (1σ , 9 hr)	10 μ Jy	1 μ Jy	10
Bandwidth per polarization	0.1 GHz	8 GHz	80
Coarsest frequency resolution	50 MHz	2 MHz	25
Finest frequency resolution	381 Hz	0.12 Hz	3180
Channels at max. bandwidth	16	16,384	1024
Maximum number of channels	512	4,194,304	8192

separately cross-correlated and integrated before being stitched together again to yield the final wideband spectrum. The new WIDAR correlator and its superior bandwidth capability provides the VLA with greater sensitivity, allowing the detection of lower flux density sources than was previously possible with the old VLA. A comparison of the performance parameters of the VLA with those of the old VLA is shown in Table 3.5. The three major new observational abilities of the VLA are:

1. Complete frequency coverage between 1 and 50 GHz.
2. An increase in continuum sensitivity by an order of magnitude at some frequencies, by increasing the bandwidth to 8 GHz per polarization.
3. Process the large bandwidth with a minimum of 16,384 spectral channels per baseline.

Apart from the addition of more feeds at the center of the reflector, the structural design of the VLA has not changed during its recent upgrade. As before it consists of 27 fully steerable alt-azimuth antennas arranged along the arms of an upside-down ‘Y’ as shown in Figure 2.9. The array is reconfigurable and can vary its resolution by over a factor of ~ 50 through movement of its component antennas along twin railroad tracks. Four standard configurations of antennas along the arms of the array are possible whose scales vary by the ratios 1 : 3.28 : 10.8 : 35.5 from smallest to largest. These are called D, C, B, and A configurations, with A having the longest baselines (~ 36 km) giving the best angular resolution, but lacking short baselines needed for imaging extended structure. In each

3.5 The Karl G. Jansky Very Large Array

configuration, the distance of each antenna from the center of the ‘Y’ is equal to $m^{\ln 2}$ where m is the antenna location number, counting outwards from the center of each arm. With this design, the m ’th station in any configuration coincides with the $2m$ ’th station in the next smaller configuration. This means that only 72 stations are needed to handle all four configurations. Additionally, there are 3 *hybrid* configurations called DnC, CnB, and BnA, which are well suited for sources with low declinations. In these configurations, the North arm antennas are deployed in the next larger configuration than the SE and SW arm antennas resulting in a more circular synthesized beam for these sources.

Each antenna is 25 m in diameter giving the array a total collecting area equivalent to a single dish of 130 m in diameter. Each antenna has an off-axis Cassegrain design with a rotatable sub-reflector at the prime focus of the main reflector and is supported by four feed legs. All feeds are located on a feed ring at the Cassegrain focus and the observing feed is changed by rotating the asymmetric sub-reflector about the main reflector axis so that the secondary focal point moves to the desired feed. The standard observing mode for all feeds is circular polarization. RF signals from each feed are sent via a waveguide to the antenna vortex room located directly underneath the main reflector where they are feed into low noise front ends. The vortex room is temperature controlled and also contains cryogenic cooling systems for the front end, portions of the LO, and IF equipment. IF signals from each antenna are sent by cable to a shielded room where the sampler and delay and multiplier racks are located. **Once the signals have been cross-correlated they are time averaged into visibility measurements.**

All VLA antennas are outfitted with eight receivers providing continuous frequency coverage between 1 and 50 GHz. As shown in Table x, the frequency ranges of 1-2 GHz, 2-4 GHz, 4-8 GHz, 8-12 GHz, 12-18 GHz, 18-26.5 GHz, 26.5-40 GHz, and 40-50 GHz, are commonly referred to as L, S, C, X, Ku, K, Ka, and Q bands, respectively. Additionally, the VLA is currently being outfitted with even lower frequency receivers, P-band (230-470 MHz) and 4-band (54-86 MHz). The VLA’s angular resolution is set by the maximum baseline B_{\max} and frequency of observation. This means that structures smaller than the diffraction limit ($\theta_{\text{HPBW}}^{\text{SB}} \sim \lambda/B_{\max}$) will be smoothed to the resolution of the array. Table x

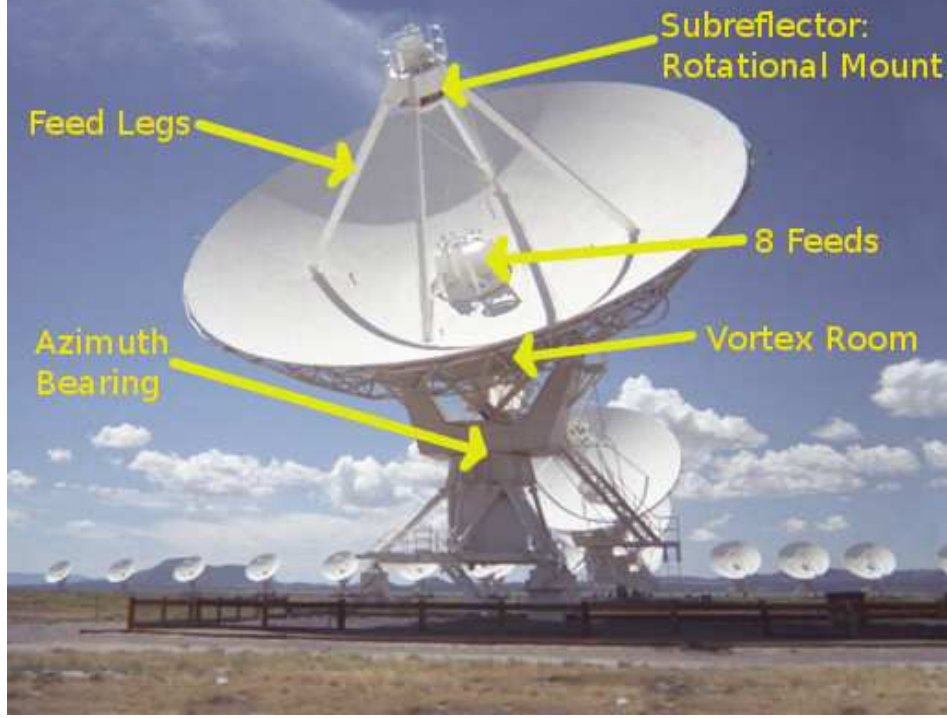


Figure 3.1: Main features of a VLA antenna. The sub-reflector is located at prime focus on a rotational mount is supported by four feed legs. The 8 feeds are located in a ring at the secondary focus. The feeds send the RF signal to the front end located in the vortex room directly beneath the main reflector.

summarizes the maximum resolution for each of the four main configurations at each wavelength. The resolution is defined here as the HPBW of the synthesized beam, using uniform weighting, over a full 12 hour synthesis observation of a source which passes near the zenith. For completeness, we also give the field of view (FOV) at each observing frequency in Table x, defined as the HPBW of the primary beam, which for the VLA antennas can be approximated using the formula: $\theta_{\text{HPBW}}^{\text{PB}}(^{\circ}) = 45/\nu_{\text{GHz}}$.

3.6 VLA Observations of Arcturus and Aldebaran

The Open Shared Risk Observing (OSRO) program at the VLA existed during its commissioning phase to provide observers with early access to a number of

3.6 VLA Observations of Arcturus and Aldebaran

Table 3.5: Frequency coverage, primary beam, and angular resolution of the VLA.

	L	S	C	X	Ku	K	Ka	Q
ν (GHz)	1.5	3.0	6.0	10	15	22	33	45
λ (cm)	20	13	6.0	3.0	2.0	1.3	1.0	0.7
ν Range (GHz)	1-2	2-4	4-8	8-12	12-18	18-26.5	26.5-40	40-50
FOV: $\theta_{\text{HPBW}}^{\text{PB}}$ (')	30	15	7.5	4.5	3.0	2.0	1.4	1.0
A config: $\theta_{\text{HPBW}}^{\text{SB}}$ (")	1.3	0.65	0.33	0.20	0.13	0.089	0.059	0.043
B config: $\theta_{\text{HPBW}}^{\text{SB}}$ (")	4.3	2.1	1.0	0.6	0.42	0.28	0.19	0.14
C config: $\theta_{\text{HPBW}}^{\text{SB}}$ (")	14	7.0	3.5	2.1	1.4	0.95	0.63	0.47
D config: $\theta_{\text{HPBW}}^{\text{SB}}$ (")	46	23	12	7.2	4.6	3.1	2.1	1.5

VLA correlator capabilities and observing modes. This represented a considerable improvement over the capabilities of the old VLA correlator as observers were provided with increased bandwidth capability at existing VLA bands, increased spectral resolution capabilities, and access to new spectral bands. In September 2010 our proposal (PI: G. M. Harper, Program ID: 10C-105) to observe two archetypical red giants at multiple frequencies was allocated the requested 15.5 hours of observing time with the VLA as part of NRAO's OSRO Science Program 2010C. A number of observing scripts called scheduling blocks (SBs) were prepared during December 2010 and their duration were kept to ≤ 2.5 hours to increase their likelihood of being scheduled. The VLA now uses dynamic scheduling for deciding which SBs are executed at any time. It takes into account many factors like the scheduling priority assigned by the time allocation committee, weather constraints, and SB duration. Dynamic scheduling means that the observer does not know when their observations will occur but in general, the chances of observations being scheduled are increased if the duration of the SB is kept short.

Table 3.6: VLA Observations of α Boo and α Tau obtained in February 2011 and July 2012.

Star	Date	Band	ν (GHz)	λ (cm)	Time on Star (hr)	Restoring Beam ($'' \times ''$)	Bandwidth (GHz)	Number of Antennas	Phase Calibrator
α Boo	2011 Feb 22	Q	43.3	0.7	0.3	0.19×0.15	0.256	22	J1357+1919
	2011 Feb 22	Ka	33.6	0.9	0.2	0.25×0.20	0.256	23	J1357+1919
	2011 Feb 22	K	22.5	1.3	0.4	0.35×0.28	0.256	24	J1357+1919
	2011 Feb 11	X	8.5	3.5	0.3	1.14×0.70	0.256	18	J1415+1320
	2011 Feb 11	C	5.0	6.0	0.5	2.02×1.30	0.256	21	J1415+1320
	2011 Feb 13	S	3.1	9.5	1.8	2.57×2.08	0.256	12	J1415+1320
	2012 Jul 19	S	3.0	10.0	0.7	2.82×2.30	2.0	23	J1415+1320
	2012 Jul 20	L	1.5	20.0	1.6	4.46×3.94	1.0	23	J1415+1320
α Tau	2011 Feb 11	Q	43.3	0.7	0.3	0.18×0.16	0.256	22	J0431+1731
	2011 Feb 11	Ka	33.6	0.9	0.2	0.22×0.20	0.256	19	J0449+1121
	2011 Feb 11	K	22.5	1.3	0.4	0.35×0.31	0.256	21	J0449+1121
	2011 Feb 13	X	8.5	3.5	0.5	0.85×0.78	0.256	25	J0449+1121
	2011 Feb 13	C	5.0	6.0	1.2	1.48×1.32	0.256	21	J0449+1121
	2011 Feb 12	S	3.1	9.5	1.8	2.74×2.02	0.256	11	J0431+2037

3.6 VLA Observations of Arcturus and Aldebaran

Our main set of observations took place in February 2011 while the VLA was in B-configuration. All observations were taken in continuum mode and the correlator was set up with two 128 MHz sub-bands centered on the frequencies listed in Table x. Each sub-band had sixty-four channels of width 2 MHz and four polarization products (RR, LL, RL, LR). We obtained all our requested observations of α Tau in just two days between the 11th and 13th of February 2011 which consisted of Q, Ka, K, X, C, and S band observations of the star. We did not request L band (i.e. 1.5 GHz) observations of α Tau as it was believed that the star would be too faint to be observable at this frequency. There was also insufficient Ku band receivers available at the time to carry out observations at 15 GHz. We obtained Q, Ka, K, X, C, and S band observations of α Boo in eleven days between the 11th and 22nd of February 2011. We also had prepared a 2.5 hour SB for α Boo at L-band but this SB was never executed.

For this reason we applied for (and were awarded) 3 additional hours of directors discretionary time (DDT) in early 2012 (PI: E. O’Gorman, Program ID: 12A-472) to observe α Boo at S and L band. We decided to include a short observation at S band even though we already had an observation at this band to make sure that the stars flux density had not significantly changed over that period and so any possible L band detection could be included in the analysis of the main set of data from the previous year. Our DDT observations took place in July 2012 when the VLA was again in B-configuration and some of these details are given in Table x. The capabilities of the VLA had greatly increased in the ~ 1.5 years since the main set of observations and we now could utilize the full 1 and 2 GHz of bandwidth at L and S band, respectively. The 1-2 GHz and 2-4 GHz frequency ranges were both divided into 16 sub-bands, each with sixty-four channels. The channel width was 2 and 1 MHz for S and L-band, respectively, and each sub-band had four polarization products (RR, LL, RL, LR).

In radio interferometry, baseline-dependent additive errors in the visibilities can occasionally lead to artifacts occurring at phase center of the final image. Such errors may be caused by unflagged low level interference picked up by some antennas baselines. An example of this is demonstrated in Figure x in which two radio images of Betelgeuse at 15 GHz are shown (A. Brown, priv. comm.). The left panel was taken on 2nd February **2002** and shows a 30σ detection of

3.6 VLA Observations of Arcturus and Aldebaran

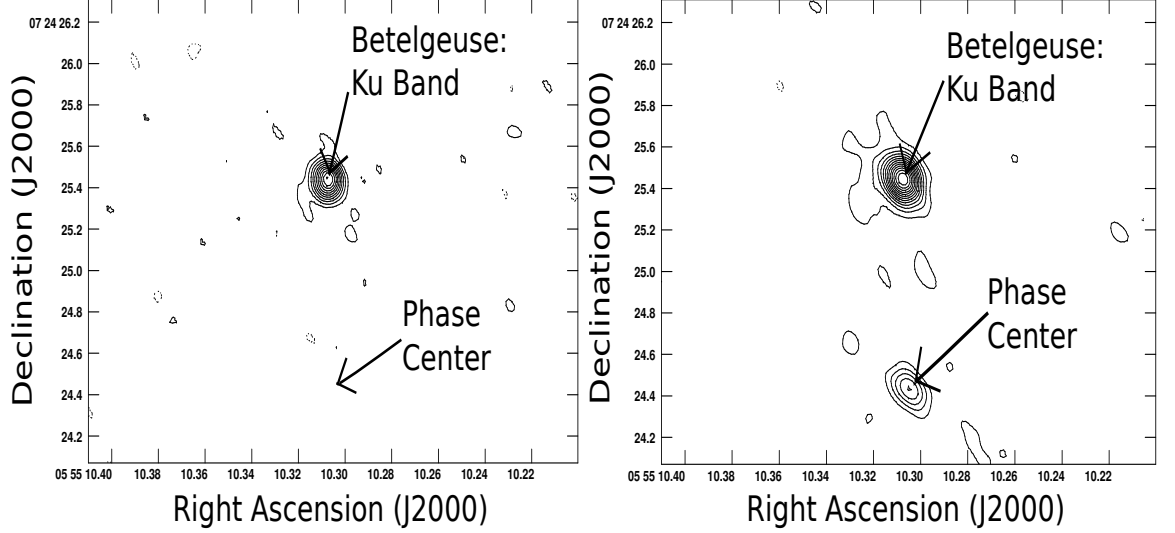


Figure 3.2: An example to highlight the importance of offsetting the source from phase center. *Left:* Old VLA image of Betelgeuse at 15 GHz taken on showing no source at the phase center of the image. Contour levels at $\sigma(-6,-3,3,...,30)$ where $\sigma = 84 \mu\text{Jy}$. *Right:* Two months later Betelgeuse was again image at 15 GHz but now shows a strong artifact at phase center. Contour levels at $\sigma(-6,-3,3,...,45)$ where $\sigma = 90 \mu\text{Jy}$ (A. Brown, priv. comm.).

Betelgeuse with low level background noise. The right panel which was taken two months later on 2nd April **2002** again shows a strong 45σ detection of the star but also now shows a 15σ artifact at phase center. If the target had been observed at phase center in this case, then this artifact would lead to an incorrect flux density measurement for the star. For our VLA observations, both α Boo and α Tau were slightly offset from the phase-center by ~ 5 synthesized beam widths in order to avoid source contamination by any phase center artifacts and to avoid spurious detections.

The main problem at low VLA frequencies (L and S bands) is disturbances in the ionosphere caused by solar activity. At L-band, solar flares can be as strong as 1×10^6 Jy and are a major source of interference, with their effects sometimes being impossible to remove from the data. To avoid such problems the S and L band SBs were scheduled for night time observing only. The low to intermediate frequency observations (L - X bands) were composed of repeatedly interleaved observations of the target and a nearby phase calibrator with cycle times of 12 minutes; 10 minutes on the target and 2 minutes on the phase calibrator. For α

3.6 VLA Observations of Arcturus and Aldebaran

Boo, the point source J1415+1320 which is located 6° away was used as the phase calibrator at these frequencies. For α Tau, the point source J0449+1121 located 6° away was used at C and X band, while the brighter J0431+2037 located 4° away was used at S band due to it being unresolved at this frequency (but is resolved at C and X band). The primary calibration sources 3C286 and 3C138 were observed at the end of all low and intermediate frequency SBs and were used to measure the bandpass and set the absolute flux for α Boo and α Tau, respectively. The top panel in Figure x shows a plot of elevation against time for all the sources observed in the SB of the C and X band observations of α Tau. In this SB, observations of α Tau at X band were interspersed between C band observations throughout the track to obtain a good spread in $u - v$ coverage.

At high VLA frequencies (i.e. K, Ka, and Q band) the troposphere can cause major phase variations to incoming radio waves. To reduce this problem, the old VLA used a technique called *fast switching* which reduced the setup overhead and slewing compared to traditional iterating between source and calibrator scans. This overhead is sufficiently reduced with the new VLA and no special fast switching mode is necessary. Instead regular but short duration source-calibrator loops are implemented. As a result, the calibration overheads for high frequency observing are typically considerably larger than for lower frequency observations. For both stars, the total cycle times for the Q, Ka, and K-band observations were 160, 230, and 290 s, respectively. These high frequency observations were combined into a single 2 hour SB for each star and commenced with X-band reference pointing with solutions being applied on-line. As mentioned in Section x, the blind pointing errors of the VLA antennas can occasionally be as large as the HPBW of the primary beam at high frequencies. Thankfully, the pointing can be calibrated for using a technique known as *reference pointing* whereby a nearby known calibrator is observed in interferometer pointing mode every hour or so. The measured local pointing corrections are then be applied to subsequent target observations. Reference pointing can reduce the rms pointing errors to as little as $2''$ if the reference source is within 10° of the target source. After X-band pointing the target source was observed at Q-band to ensure the best pointing solutions were used as shown in the lower panel of Figure x for α Tau.

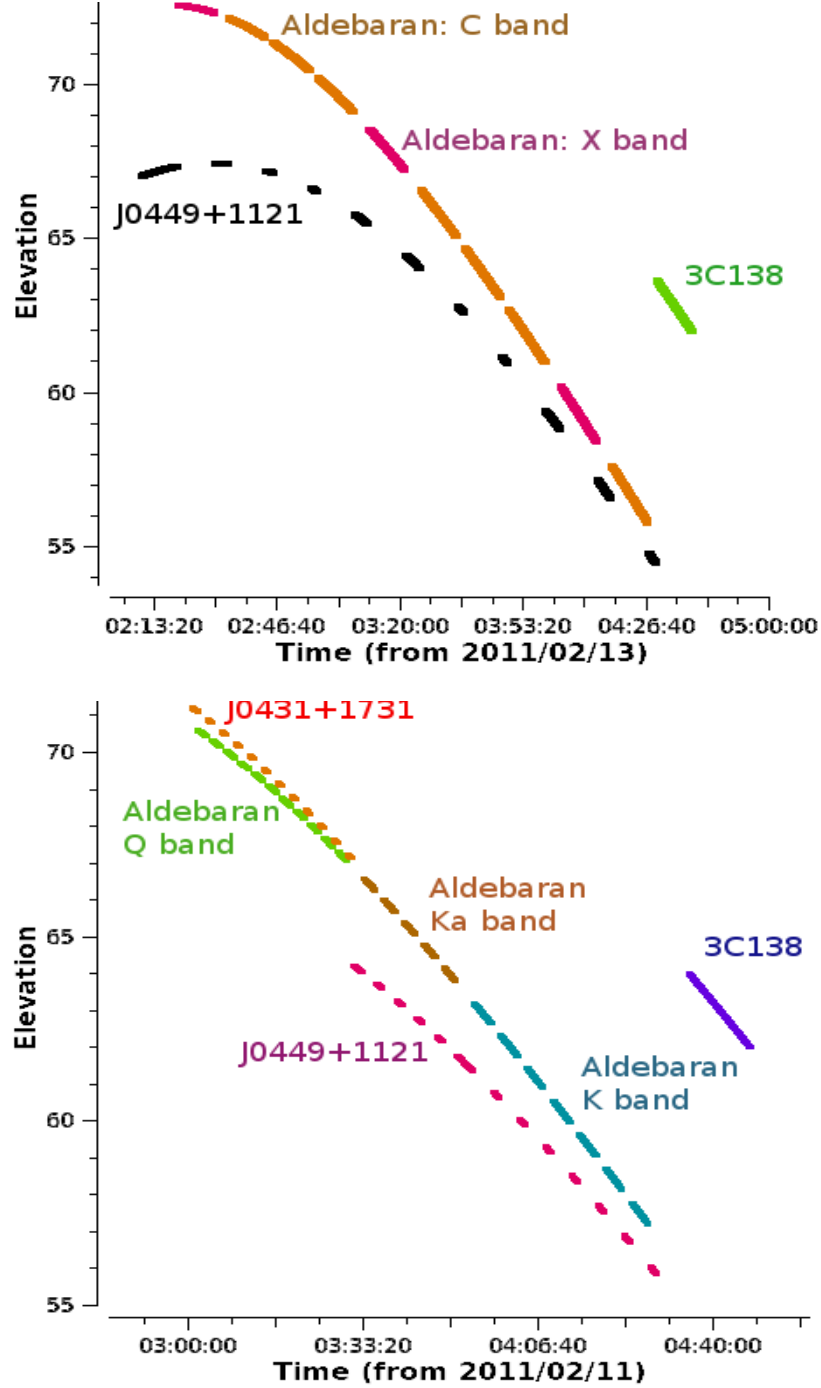


Figure 3.3: Overview of a low and high frequency VLA SB for α Tau. *Top Panel:* The low frequency observations consisted of interleaved observations of the target and a nearby phase calibrator with cycle times of 12 minutes. The X band observations were interspersed between C band observations to obtain a good spread in $u-v$ coverage. *Bottom Panel:* The high frequency observations had short cycle times to compensate for tropospheric effects. Q band observations were taken first to ensure the best pointing solutions were applied to them.

4

Data Analysis

4.1 Measurement Equation

5

CARMA CO($J = 2 - 1$) Observations of the Circumstellar Envelope of Betelgeuse

5.1 Introduction

6

Multi-wavelength Radio Continuum Emission Studies of Dust-free Red Giants

6.1 Introduction

6.2 α Boo Radio Maps

6.3 α Tau Radio Maps

6.4 Results vs Previous Observations

Prior to and during the early operation of the ‘old’ VLA, a small number of single dish radio observations reported the detection of flares from single red giants (e.g., [Slee *et al.* 1989](#)). These transient radio events have never been re-observed however, even with more sensitive interferometers, suggesting that such detections were spurious (e.g., [Beasley *et al.* 1992](#)). The first definitive detection of thermal free-free emission from a luminosity class III single red giant at centimeter wavelengths was of α Boo at 6 cm ([Drake & Linsky, 1986, 1983](#)). Since then

6.4 Results vs Previous Observations

there has been a modest number of centimeter and millimeter observations of this star. In Table 6.1 we list the majority of these observations and plot their flux densities as a function of frequency in Figure x. In comparison to other single red giants, α Boo had been relatively well observed at radio continuum wavelengths before this study, including detections in four VLA bands (i.e., Q, K, Ku, and C). No Ku band receivers were available during the commissioning phase of the VLA in early 2011 so we can compare three of our detections with previous ones.

Table 6.1: Compilation of Previous Radio Observations ($\nu \leq 250$ GHz).

Source	ν (GHz)	Date	F_ν (mJy)	S/N	Reference
α Boo	4.9	1983 Jan 21	0.39	3.0	1
	4.9	1983 May 20	0.26	3.3	1
	4.9	1983 Dec 26	$\leq 0.18(3\sigma)$	-	1
	4.9	1984 Mar 17	0.24	4.8	1
	15.0	1984 Nov 6	0.68	7.6	1
	22.5	1999 Jan 06	1.7	8.5	2
	43.3	1999 Jan 06	3.3	8.3	2
	43.3	2004 Jan 25	3.34	41.8	2
	86.0	1985 Nov	21.4	3.0	3
	108.4	1997 Nov - 2000 Jun	20.1	29.1	4
	217.8	1997 Nov - 2000 Jun	83.5	48.8	4
	250.0	1986 Dec - 1989 Mar	78.0	9.8	5
α Tau	4.9	1983 Jan 21	$\leq 0.27(3\sigma)$	-	1
	4.9	1984 Nov 6	$\leq 0.22(3\sigma)$	-	1
	5.0	1997 Sep 27	$\leq 0.07(3\sigma)$	-	6
	8.5	1997 Sep 27	0.28	9.3	6
	14.9	1997 Sep 27	0.95	11.9	6
	15.0	1984 Nov 6	0.60	6.0	1
	108.4	1997 Nov - 2000 Dec	14.0	9.6	4
	217.8	1999 Sep - 2000 Dec	25.8	4.6	4
	250.0	1986 Dec - 1987 Jan	51.0	8.5	5

References.-(1) Drake & Linsky (1986); (2) Dehaes *et al.* (2011); (3) Altenhoff *et al.* (1986); (4) Cohen *et al.* (2005); (5) Altenhoff *et al.* (1994); (6) Wood *et al.* (2007);

Previous detections of α Boo at 6 cm ranged from a 3σ upper limit of 0.18

mJy to a 3σ detection at 0.39 mJy. Our 6 cm value agrees to within $\sim 10\%$ of the highest S/N (5σ) value of Drake & Linsky (1986). There is no significant difference between our 1.3 cm value and that of Dehaes *et al.* (2011). There is however a notable difference in flux density values at 0.7 cm where Dehaes *et al.* (2011) report values that are lower than ours by over 40%. Such a level of chromospheric variability seems rather high and would be unexpected from such supposedly inactive stars (Harper *et al.*, 2013). Another possibility for the difference in values is that the longer cycle time used by Dehaes *et al.* (2011), which was over double our value, may lead to larger phase errors and thus lower final flux density values. Future high frequency VLA observations of α Boo will clarify this discrepancy at 0.7 cm but past detections at longer wavelengths appear to be in good agreement with our data.

In Figure x we plot the previous radio measurements of α Tau at all frequencies below 250 GHz (i.e. 0.12 cm). Prior to this study, α Tau had only been detected at two VLA bands (i.e., X and Ku) and had never been detected at wavelengths longer than 3 cm due to its relatively low mass-loss rate. Our lack of a Ku-band measurement means that we can only compare the previous 3 cm detection reported in Wood *et al.* (2007) to ours. We find that there is no significant difference between the two. Interestingly, Wood *et al.* (2007) report a non-detection of α Tau at 6 cm and placed a 3σ upper limit of 0.07 mJy on its emission. In stark contrast to this, we were able to detect the star at 6 cm with a flux density over two times greater than this value. This hint of variability at long wavelengths would be consistent with the predictions of the broadband nonlinear Alfvén wave model of Airapetian *et al.* (2010) but can only be confirmed with future high S/N observations.

6.5 Results vs Existing Models

6.6 Constraining α Tau’s Molsphere

Recently, Ohnaka (2013) has detected a layer of CO in the outer atmosphere of α Tau (i.e. a so-called MOLsphere) which extends out to $\sim 2.5 R_\star$, has a temperature of 1500 ± 200 K, and a CO column density of $\sim 1 \times 10^{20} \text{ cm}^{-2}$. They

6.7 Estimation of Mass Loss Rates from the Radio Data

were unable to constrain the geometrical thickness, ΔL , of the MOLsphere from the data however, and arbitrarily fixed it to $0.1 R_\star$. It can be shown that such a MOLsphere would have an optical depth of $\tau_{6\text{ cm}} = 4.6$ at C-band and would produce a corresponding flux density of 0.06 mJy which is considerably lower than our high S/N measurement of 0.15 mJy. Here, we have conservatively assumed that the electrons in this region of the atmosphere come from singly ionized metals and have an abundance of $\sim 1 \times 10^{-5} n_{\text{H}}$, where n_{H} is the total hydrogen number density. We have also assumed the CO filling factor to be unity. It can also be shown that the MOLsphere becomes optically thin at C-band (i.e. $\tau_{6\text{ cm}} < 1$) for $\Delta L > 0.45 R_\star$. In the next section we argue that the radio emission from α Tau even at long VLA wavelengths comes from a region much closer in to the star which suggests that the MOLsphere either has a geometrical width $> 0.45 R_\star$ or has a filling factor less than unity.

6.7 Estimation of Mass Loss Rates from the Radio Data

Free-free radio emission from the atmospheres of red giants is only sensitive to the ionized component of the outflow. Non-coronal and hybrid atmosphere red giants have only partially ionized atmospheres and so we are only ever capable of finding a lower limit on the mass loss rate from their thermal continuum radio emission. Nevertheless, it is a sufficiently worthwhile goal and can test the validity of existing values obtained from optically thick emission lines in the UV or optical regime.

For a partially ionized outflow, such as that expected from α Boo and α Tau, the ionized mass loss rate can be estimated from the radio emission assuming a constant velocity, constant temperature, and constant ionization fraction and can be written as

$$\begin{aligned} \dot{M}_{\text{ion}} \simeq & 5.58 \times 10^{-14} \left(\frac{v_\infty}{\text{km s}^{-1}} \right) \left(\frac{D}{\text{pc}} \right) \left(\frac{F_\nu}{\text{mJy}} \right)^{0.75} \\ & \times \left(\frac{\lambda}{\text{cm}} \right)^{0.45} \left(\frac{T_e}{10^4 \text{K}} \right)^{0.1} \dot{M}_\odot \text{ yr}^{-1} \end{aligned} \quad (6.1)$$

where D is the distance and v_∞ is the wind terminal velocity defined earlier in Table ???. Using this expression, the ionized mass loss rates were derived for each of the long wavelength measurements for both stars and are listed in Table ??. These values are based on the assumption of a $T_e = 10^4$ K wind for both stars.

Table 6.2: Ionized mass loss rates for α Boo and α Tau.

Star	Wavelength (cm)	$\dot{M}_{\text{ion}} (M_\odot \text{ yr}^{-1})$
α Boo	6.0	5.9×10^{-11}
	9.5	5.5×10^{-11}
	10.0	5.1×10^{-11}
	20.0	4.3×10^{-11}
α Tau	6.0	$\leq 8.2 \times 10^{-11}$
	9.5	$\leq 5.3 \times 10^{-11}$

We have have discussed in the previous sections that for α Boo, these long wavelengths sample the outer atmosphere of the star where the wind is close to or has reached its terminal velocity and is beginning to cool due to gas expansion. In this case, these \dot{M}_{ion} values would be lower than those given in ??. However, as \dot{M}_{ion} is only weakly dependent on T_e this makes only a small difference and amounts to about a 7% increase in the ionized mass loss if the temperature is actually lower by 50%. If the ionization balance is frozen-in in the regions of the outflow where these long wavelengths sample then the derived \dot{M}_{ion} should be the same for these wavelengths. The decrease in \dot{M}_{ion} with longer wavelengths as seen in Table ?? is probably therefore due to a combination of lower temperatures and lower ionization fractions further out in the atmosphere. The ionized mass loss rates for α Tau given in Table ?? are derived assuming the radio emission emanates from the outer atmosphere where the wind has reached its terminal velocity. As discussed in Section ?? the longest wavelengths are still sampling the acceleration zone and thus these ionized mass loss rates are just upper limits.

6.8 Spectral Indices

Long wavelength radio emission from non-dusty K spectral-type red giants is due to thermal free-free emission in their partially ionized outflows while shorter

wavelength radio emission emanates from the near static and more ionized lower atmospheric layers. The radio flux density-frequency relationship for these stars is usually found to be intermediate between that expected from the isothermal stellar disk emission, where α follows the Rayleigh-Jeans tail of the Planck function (i.e., $\alpha = +2$), and that from an optically thin plasma (i.e., $\alpha = -0.1$). We have shown in Chapter 1 that the expected radio spectrum from a spherically symmetric isothermal outflow with a constant velocity and ionization fraction varies as $\nu^{0.6}$ (Olnon, 1975; Panagia & Felli, 1975; Wright & Barlow, 1975). In reality however, thermal gradients will exist in the outflow when the heating mechanisms become insufficient to counteract adiabatic and line cooling, so one would expect a temperature decrease in the wind at some point. Also, if the radio emission emanates from the wind acceleration zone then the electron density will not follow $n_e \propto r^{-2}$.

We therefore relax some of the constant property wind model assumptions and assume that the electron density and temperature vary as a function of distance from the star r , and have the power-law form $n_e \propto r^{-p}$ and $T_e \propto r^{-n}$, respectively (e.g., Seaquist & Taylor, 1987). Finding the spectral index for an outflow with these conditions is non-trivial so we highlight the main steps required to do so here. We assume the same geometry and notation used for the constant property wind model in Chapter 1, and again start by calculating the total optical depth for a ray with an impact parameter b , through the atmosphere:

$$\tau_\nu = \frac{0.212 Z^2 n_e^2(r_0) r_0^{2p}}{T_e^{1.35} \nu^{2.1} T_e^{1.35}(r_0) r_0^{1.35n}} \int_{-\infty}^{\infty} \frac{1}{(b^2 + z^2)^{(1.35n-2p)/2}} dz. \quad (6.2)$$

This integral can be solved using the relationship

$$\int_{-\infty}^{\infty} \frac{1}{(b^2 + z^2)^{t/2}} dz = b^{1-t} \sqrt{\pi} \left[\frac{\Gamma(0.5t - 0.5)}{\Gamma(0.5t)} \right] \quad (6.3)$$

and setting $t = (1.35n - 2p)$. Here Γ is the gamma function i.e., $\Gamma(y) = \int_0^\infty u^{y-1} e^{-u} du$. The total optical depth along a ray is then

$$\tau_\nu(b) = G b^{1-2p+1.35n} \quad (6.4)$$

where G is a constant that incorporates ν . As the total flux density is

$$F_\nu = \frac{2\pi}{D^2} \int_0^\infty B_\nu [1 - e^{-\tau_\nu(b)}] b db, \quad (6.5)$$

we can now substitute in the Rayleigh Jeans function for B_ν (remembering that T_e now depends on distance from the star) to get

$$F_\nu = \frac{4\pi k \nu^2 T_e(r_0) r_0^n}{D^2 c^2} \int_0^\infty (1 - e^{-\tau_\nu}) (b^2 + z^2)^{-\frac{n}{2}} b db. \quad (6.6)$$

Expansion of the second term inside the integral gives

$$F_\nu \simeq \frac{4\pi k \nu^2 T_e(r_0) r_0^n}{D^2 c^2} \int_0^\infty (1 - e^{-\tau_\nu}) b^{1-n} db. \quad (6.7)$$

To progress further, Equation 6.4 can be rearranged to find b and db in terms of τ_ν , and can then be inserted into Equation 6.7 to give

$$F_\nu \simeq \frac{4\pi k \nu^2 T_0(r_0) r_0^n}{D^2 c^2} \int_0^\infty (1 - e^{-\tau_\nu}) \left(\frac{\tau_\nu}{G} \right)^{\frac{1-2.35n+2p}{1-2p+1.35n}} \frac{d\tau_\nu}{G(1-2p+1.35n)}. \quad (6.8)$$

This allows ν to be separated out to give

$$F_\nu \propto \nu^2 G^{\frac{2.35n-2p-1}{1-2p+1.35n}} G^{-1} \quad (6.9)$$

and as $G \propto \nu^{-2.1}$ we get

$$F_\nu \propto \nu^2 \nu^{\frac{4.2-2.1n}{1-2p+1.35n}}, \quad (6.10)$$

i.e.,

$$\alpha = \frac{4p - 6.2 - 0.6n}{2p - 1 - 1.35n}. \quad (6.11)$$

Therefore, if the spectral index of a stellar outflow can be measured, and if we make an assumption about the property of either the thermal or electron density profile of the wind, then Equation 6.11 provides us with information on how the other value varies.

The radio spectra for both stars are shown in Figure 6.1, together with the power laws that were fitted to the long wavelength flux densities by minimizing the chi-square error statistic. For α Boo, a power law with $F_\nu \propto \nu^{1.05 \pm 0.05}$ fits the four longest wavelength data points well. This spectral index is larger than

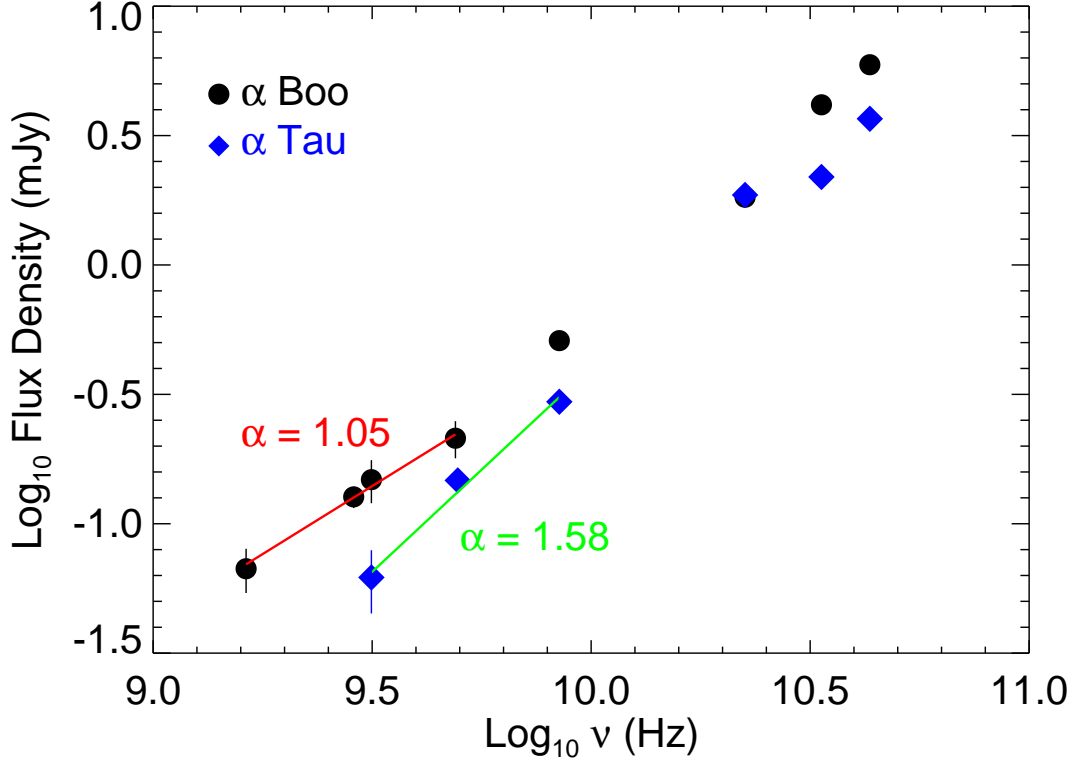


Figure 6.1: Radio spectra for α Boo and α Tau, together with the best fit power law to their long wavelength flux densities and the resulting spectral indices. The spectral indices for α Boo and α Tau are found to be 1.05 and 1.58, respectively, which are both larger than the 0.6 value expected for a constant property wind model.

the 0.8 value obtained by [Drake & Linsky \(1986\)](#) whose value was based on a shorter wavelength (2 cm) value and a mean value of four low S/N measurements at 6 cm. α Tau was found to have a larger spectral index and a power law with $S_\nu \propto \nu^{1.58 \pm 0.25}$ best fitted the three longest wavelength data points. This value is in agreement with [Drake & Linsky \(1986\)](#) who report a value ≥ 0.84 and is lower than the value of 2.18 that can be derived from the shorter wavelength data given in [Wood *et al.* \(2007\)](#). It should be emphasized that the spectral index for both stars is a lot steeper than that expected from the constant property wind model.

Equation 6.11 can be used in conjunction with our new spectral index for each star to calculate the density and temperature coefficients that may describe their

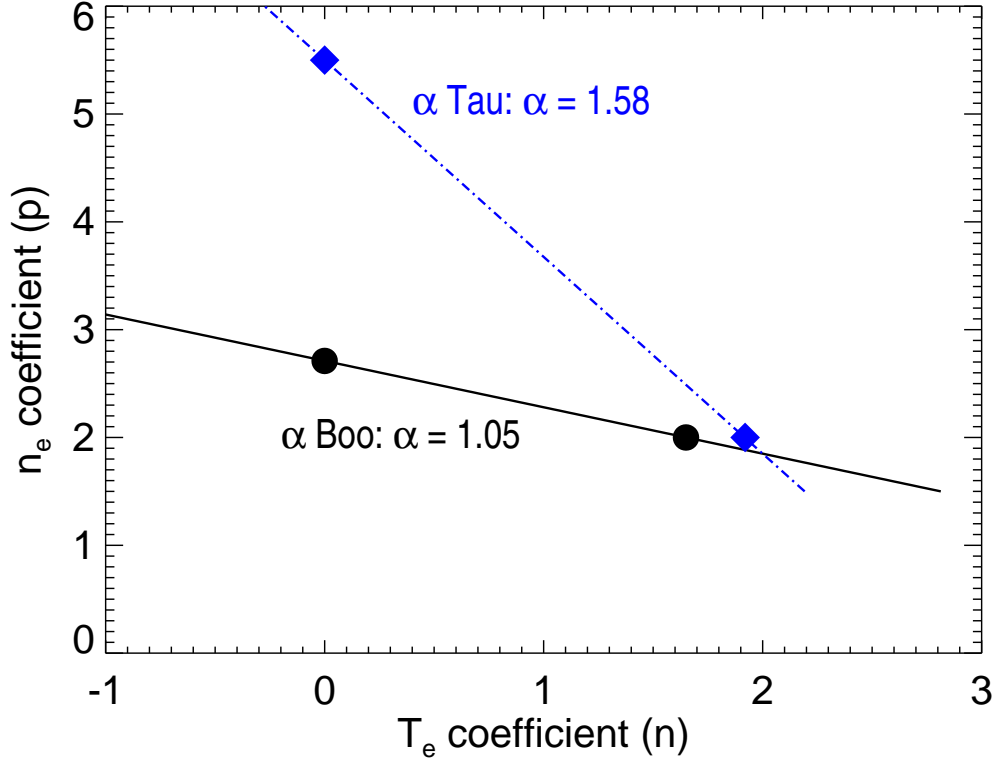


Figure 6.2: The variation of density and temperature coefficients for the empirically derived spectral indices. The density coefficients for an isothermal flow ($n=0$) along with the temperature coefficients for a constant outflow velocity ($p=2$) are also shown for both stars.

outflows. The combinations of the electron temperature and density coefficients are shown for each star in Figure 6.2 along with the coefficients obtained by assuming either an isothermal flow or a constant velocity flow. One explanation for spectral indices of stellar outflows being larger than 0.6 is that the wind is still accelerating in the radio emitting region, if the thermal gradients are assumed to be small. Ignoring thermal gradients may be reasonable over the wind acceleration region since it is probable that some form of Alfvén waves are required to lift the material out of the gravitational potential. These waves would need to have large damping lengths and undergo some dissipation within a few stellar radii of the surface in order to produce the low terminal velocities (Hartmann & MacGregor, 1980). These large damping lengths could result in

shallow thermal gradients close in. If we ignore thermal gradients, then the density coefficients are $p = 2.71$ and 5.5 for α Boo and α Tau, respectively. This assumption is reasonable at short wavelengths where the majority of the radio emission is expected to emanate from the chromosphere or wind acceleration zone, but at long VLA wavelengths (i.e., between 6 and 20 cm) we may indeed be sampling the wind very close to or at its terminal velocity and the wind may have substantial thermal gradients caused by adiabatic expansion cooling.

To investigate this matter further, we estimate the effective radius of the radio emitting region as a function of wavelength based on the Drake model for α Boo and the hybrid McMurry and Robinson model for α Tau. We follow the approach used by [Cassinelli & Hartmann \(1977\)](#) and assume that the radio emission at each wavelength emanates from a surface at radial optical depth $\tau_{\text{rad}} = 1/3$. This is a modification of the Eddington-Barbier relation for an extended atmosphere where emission from smaller optical depths has added weight. Since the radio free-free opacity increases at longer wavelengths the optical depth along a line of sight into the stellar outflow also increases at longer wavelengths. This implies that the effective radius (i.e., the radius where $\tau_{\lambda} = \tau_{\text{rad}}$) will increase with longer wavelengths and will be greater for outflows with higher densities of ionized material as $\tau_{\lambda} \propto \lambda^{2.1} \int n_{\text{ion}}(r) n_{\text{e}}(r) dr$.

The large mass loss rate of α Boo in comparison to α Tau means that the latter has a substantially smaller effective radius at longer wavelengths, as seen in Figure 6.3. At 6, 13, and 20 cm the effective radius of α Boo at $\tau_{\text{rad}} = 1/3$ is predicted to be 1.6, 2.8, and $3.7 R_{\star}$ but is only $\sim 1.2 R_{\star}$ at 6 and 13 cm for α Tau. [Robinson et al. \(1998\)](#) predict that α Tau's wind reaches $\sim 80\%$ of its terminal velocity by $3 R_{\star}$, but even our longest-wavelength observations are highly unlikely to sample the wind outside the lower velocity layers closer to the star. For α Boo however, [Drake \(1985\)](#) predicts that the wind has reached its terminal velocity by $\sim 2 R_{\star}$, so based on this model our longest-wavelength measurements are of the region where the wind has reached a steady terminal velocity. From Figure 6.3, this implies that the n_{e} coefficient is $p = 2$ and thus the T_{e} coefficient is $n = 1.65$. Pure adiabatic cooling with no heat source has $n = 1.33$ so additional cooling routes must be operating, possibly due to recombination of H^{+} and/or line cooling. Finally, the wind ionization balance may not have become *frozen-in*

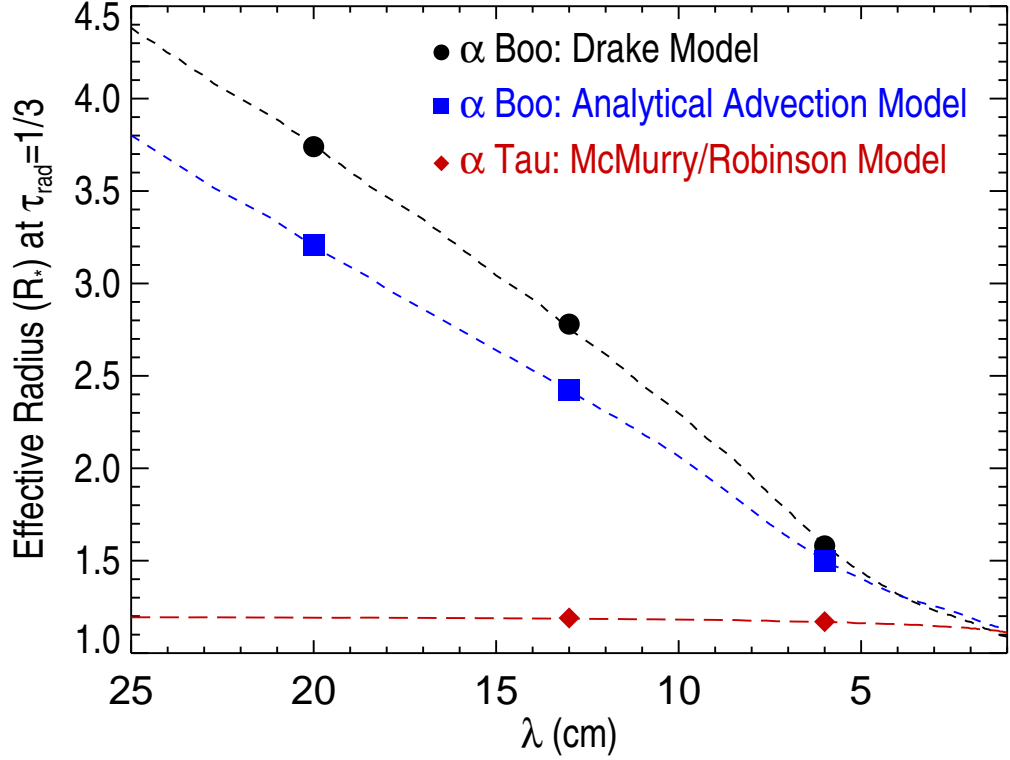


Figure 6.3: Predicted effective radius (dashed lines) as a function of wavelength derived from the existing atmospheric models of α Boo and α Tau. Also plotted is the predicted effective radius derived from our analytical advection model for α Boo (discussed in Section 6.9). Points corresponding to our long wavelength VLA measurements are also shown. At the same radio wavelengths the lower mass loss rate of α Tau’s outflow results in a smaller effective radius than that for α Boo.

in the region of α Boo’s wind where the radio emission emanates from. If this is true, then the excess slope of the spectral index could be due to a combination of both cooling and changing ionization fraction. In this scenario the temperature coefficient n , would be smaller than our derived value because Equation 6.11 assumes a constant ionization fraction.

6.9 Analytical Advection Model for α Boo's Wind

A failure of the Drake model for α Boo is that it overestimates our long wavelength VLA radio flux densities which sample the outer atmosphere, as clearly shown in Figure x. If these wavelengths are indeed sampling the wind at its terminal velocity then one reason for this overestimation is that the wind is cooling closer in than predicted by the existing model, which assumes a constant temperature of 8,000 K out to $\sim 20 R_\star$. The main mechanism for such cooling would be adiabatic expansion (O’Gorman & Harper, 2011) and would cause lower electron densities than those predicted by the existing model due to larger recombination rates. In the next two sections we derive the fractional ionized hydrogen in a stellar outflow with a temperature gradient based on the work of Glassgold & Huggins (1986), and use this method to insert a temperature gradient into the outer atmosphere of the Drake model to see if such an atmosphere could match our new long wavelength VLA flux densities better.

6.9.1 H II recombination in a stellar outflow

The time dependent non-static rate/statistical equations can be written as

$$\frac{\partial n_i}{\partial t} + \nabla \cdot (n_i v) = \sum_{i \neq j}^n n_j P_{ji} - n_i \sum_{i \neq j}^n P_{ij} \quad (6.12)$$

where v is the flow velocity, $n_{i,j}$ are the population densities of the energy levels i, j which are functions of radial distance r , and $P_{ij} = C_{ij} + R_{ij}$ are the total transition probabilities (s^{-1}) from energy levels $i \rightarrow j$. C_{ij} are the total collision rates (electrons, protons, and ions), and R_{ij} are the problematic radiative rates. In 1-D spherical geometry

$$\nabla \cdot A = \frac{1}{r^2} \frac{d}{dr} (r^2 A) \quad (6.13)$$

6.9 Analytical Advection Model for α Boo's Wind

where A is some vector quantity and equals $n_i v$ in our case. Thus, for a steady flow the rate equations become

$$\frac{1}{r^2} \frac{d}{dr} (r^2 v n_{\text{tot}} \frac{n_i}{n_{\text{tot}}}) = \sum_{i \neq j}^n n_j P_{ji} - n_i \sum_{i \neq j}^n P_{ij} \quad (6.14)$$

where n_{tot} is the total hydrogen number density (i.e. $n_{\text{tot}} = n_{\text{HI}} + n_{\text{HII}}$). We note that $r^2 v n_{\text{tot}}$ is some constant of the flow defined by the mass continuity equation, and if we define the relative populations as $x_i = n_i / n_{\text{tot}}$ we get

$$v \frac{d}{dr} (x_i) = \sum_{i \neq j}^n x_j P_{ji} - x_i \sum_{i \neq j}^n P_{ij}. \quad (6.15)$$

To simplify Equation 6.15 further, we follow the approach of [Glassgold & Huggins \(1986\)](#) and assume:

1. A constant velocity mass outflow, i.e., $n_{\text{tot}} = C/r^2$ where C is a constant proportional to the ratio of the mass loss rate divided by the terminal velocity.
2. All hydrogen ionization processes cease beyond some distance r_1 (i.e. $P_{ij} = 0$). The ionization of hydrogen in the chromosphere and wind is a two stage process: the $n = 2$ level is excited by electron collisions and Lyman-alpha scattering, followed by photoionization by the optically thin Balmer continuum. When the temperature begins to decrease in the wind the collisional excitation rate and thus ionization rate decrease rapidly.
3. Only radiative recombination of hydrogen is considered [i.e. $R_{ji} = \alpha_{\text{rr}}(T_e) n_e$ where α_{rr} is the total radiative recombination coefficient].
4. A fixed ion contribution from metals with a low first ionization potential, $x_{\text{ion}} = n_{\text{ion}} / n_{\text{tot}}$, as these are easily ionized in the outflow. The total electron density is then $n_e = n_{\text{tot}} x_{\text{HII}} + n_{\text{tot}} x_{\text{ion}}$ where $x_{\text{HII}} = n_{\text{HII}} / (n_{\text{HI}} + n_{\text{HII}})$.

Using these assumptions Equation 6.15 becomes

$$\frac{dx_{\text{HII}}}{dr} = \frac{\alpha_{\text{rr}} C}{v r^2} (x_{\text{HII}}^2 + x_{\text{ion}} x_{\text{HII}}) \quad (6.16)$$

which can be rearranged and integrated between r_1 and r to give

$$\int_{x_{\text{HII}}(r_1)}^{x_{\text{HII}}(r)} \frac{dx_{\text{HII}}}{x_{\text{HII}}(x_{\text{HII}} + x_{\text{ion}})} = \int_{r_1}^r \frac{\alpha_{\text{rr}} C}{v r^2} dr. \quad (6.17)$$

6.9 Analytical Advection Model for α Boo's Wind

The ionization fraction beyond r_1 is then given by

$$x_{\text{HII}}(r) = \frac{x_{\text{HII}}(r_1)x_{\text{ion}}e^{-I(r)}}{x_{\text{ion}} + x_{\text{HII}}(r_1)[1 - e^{-I(r)}]} \quad (6.18)$$

where

$$I(r) = \int_{r_1}^r \frac{x_{\text{ion}}\alpha_{\text{rr}}C}{vr^2} dr \quad (6.19)$$

If we further assume a constant velocity, $T_e \propto r^{-n}$, and $\alpha_{\text{rr}} \propto T_e^{-\beta}$ giving $\alpha_{\text{rr}} \propto r^{-n\beta}$, then

$$x_{\text{HII}}(r) = \frac{x_{\text{HII}}(r_1)x_{\text{ion}}e^{-I(r)}}{x_{\text{ion}} + x_{\text{HII}}(r_1)(1 - e^{-I(r)})} \quad (6.20)$$

where

$$I(r) = w \left[1 - \left(\frac{r_1}{r} \right)^{1-n\beta} \right] \quad (6.21)$$

and

$$w = \frac{x_{\text{ion}}\alpha_{\text{rr}}(r_1)C}{vr_1(1 - n\beta)}. \quad (6.22)$$

As w is just a constant, $I(r)$ approaches a constant value for large r . This means that $x_{\text{HII}}(r)$ also approaches a constant value for large r , and the ionization fraction gets *frozen-in*. This is a universal property of all stellar winds. **How does it depend on \dot{M} and v ? Maybe add a plot.**

6.9.2 Application to α Boo's Wind

To investigate the possibility that α Boo's wind may be undergoing more rapid cooling closer in to the star than originally predicted by the Drake Model, we adjust one of the existing models [referred to as 'Model A' in Drake (1985)] to include a temperature power-law falloff of the form

$$T_e(r) = T_e(r_1) \left(\frac{r_1}{r} \right)^n, \quad (6.23)$$

at some distance r_1 from the star. We set the temperature coefficient to the value obtained from our new VLA data which was derived assuming a constant velocity flow, i.e. $n = 1.65$ (see Figure 6.2). We introduce the distance r_1 as the outer limit to ionization processes; at $r > r_1$, the ionization fraction is only determined by recombination. To calculate the new electron densities in the wind regime

6.9 Analytical Advection Model for α Boo's Wind

where this temperature falloff occurs, we use Equations 6.20, 6.21, and 6.22 to calculate the hydrogen ionization fraction, $x_{\text{HII}} = n_{\text{HII}}/n_{\text{H}}$. We assume a fixed ion contribution from metals with a low first ionization potential of $x_{\text{ion}} = 1 \times 10^{-4}$. So, knowing that the total hydrogen density does not change, the electron density at any point in the wind post r_1 can be found by the following formula

$$n_e(r) = n_{\text{tot}}(r)[x_{\text{HII}}(r) + 1 \times 10^{-4}]. \quad (6.24)$$

Using the same wind terminal velocity as that used in ‘Model A’ (i.e. 35 km s⁻¹) and the mass loss rate defined in Table x, we find the constant proportional to the ratio of the mass loss rate divided by the terminal velocity to be $C = 1.7 \times 10^{32} \text{ cm}^{-1}$ for α Boo. To calculate the temperature dependent radiative recombination coefficient α_{rr} and its power law coefficient β used in Equation 6.22, we consider only radiative recombination of hydrogen and exclude captures to the n=1 level. [Spitzer \(1978\)](#) has tabulated values for the variation of this recombination coefficient with temperature and it is often referred to as α_B in the literature when captures to the n=1 level are excluded. To find the power law form of α_B we found the best fit to the tabulated data between a *reasonable* range of temperatures in the outflow of α Boo. This approach is shown in Figure 6.4, where β was found to be 0.77 by fitting a power law to values of α_B between 1,000 and 16,000 K. For completeness, we also show in Figure 6.4 the slight variation in β if a wider range of temperatures is used and also if captures to the n=1 level are included. It can then be easily shown that the ionization fraction beyond r_1 is given by

$$x_{\text{HII}}(r) = \frac{x_{\text{HII}}(r_1)x_{\text{ion}}e^{-I(r)}}{x_{\text{ion}} + x_{\text{HII}}(r_1)[1 - e^{-I(r)}]} \quad (6.25)$$

where

$$I(r) = \frac{4.7 \times 10^9}{r_1} \left[\left(\frac{r_1}{r} \right)^{-0.27} - 1 \right], \text{ and } r \geq r_1. \quad (6.26)$$

We then adjusted the value of r_1 to obtain the best fit to our long wavelength observations and found this happened when $r_1 = 2.3 R_\star$. To get this best fit, the existing atmospheric model (plotted in Figure x) needed to be adjusted so that it now has a narrower and slightly larger temperature plateau of $T_e = 10,000 \text{ K}$ between 1.2 and 2.3 R_\star , and a temperature profile and a density profile governed

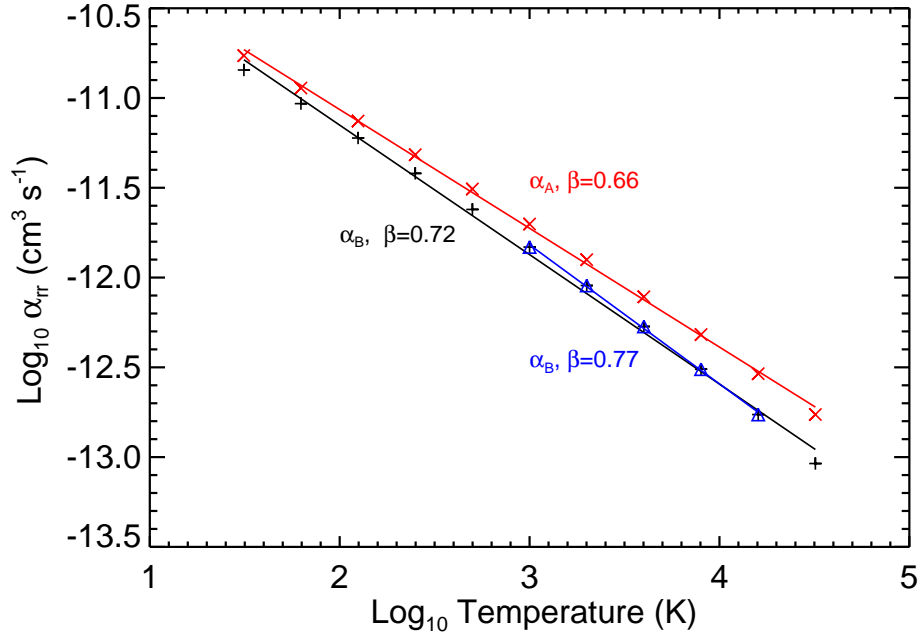


Figure 6.4: The temperature dependent recombination rates for hydrogen. The variation of the recombination rate excluding captures to the $n=1$ level α_B , with temperature is derived for the tabulated temperatures in [Spitzer \(1978\)](#) (black) and for the more realistic temperatures existing in α Boo's outflow (blue). We also show the how the recombination coefficient varies with temperature if captures to the $n=1$ level are included (red).

by Equation 6.23 and Equation 6.25 beyond $r_1 = 2.3 R_\star$, respectively. This gives much better agreement with our new long wavelength VLA data as shown in Figure x. This new *hybrid* atmospheric model which is plotted along with the original Drake model in Figure x, still has the original ionization fraction of $x_{\text{HII}} \approx 0.5$ inside $2.3 R_\star$ but now contains an initial rapid decrease in x_{HII} beyond $2.3 R_\star$ which then *freezes-in* to a constant value of ~ 0.04 beyond $\sim 10 R_\star$.

Encouraging as it is that such a simple analytical model can reproduce values close to the observed radio fluxes at long wavelengths, it must be stressed that this *hybrid* model is just a first order approximation. It assumes that the excess slope from the radio spectrum is a result of rapid cooling only. It still does not reproduce the radio fluxes at wavelengths shorter than ~ 3 cm and therefore a new atmospheric model is still required that can reproduce all of the observed flux

6.9 Analytical Advection Model for α Boo's Wind

densities. To do so, the non-trivial task of simultaneously solving the radiative transfer equation and non-LTE atomic level populations which include advection will be required.

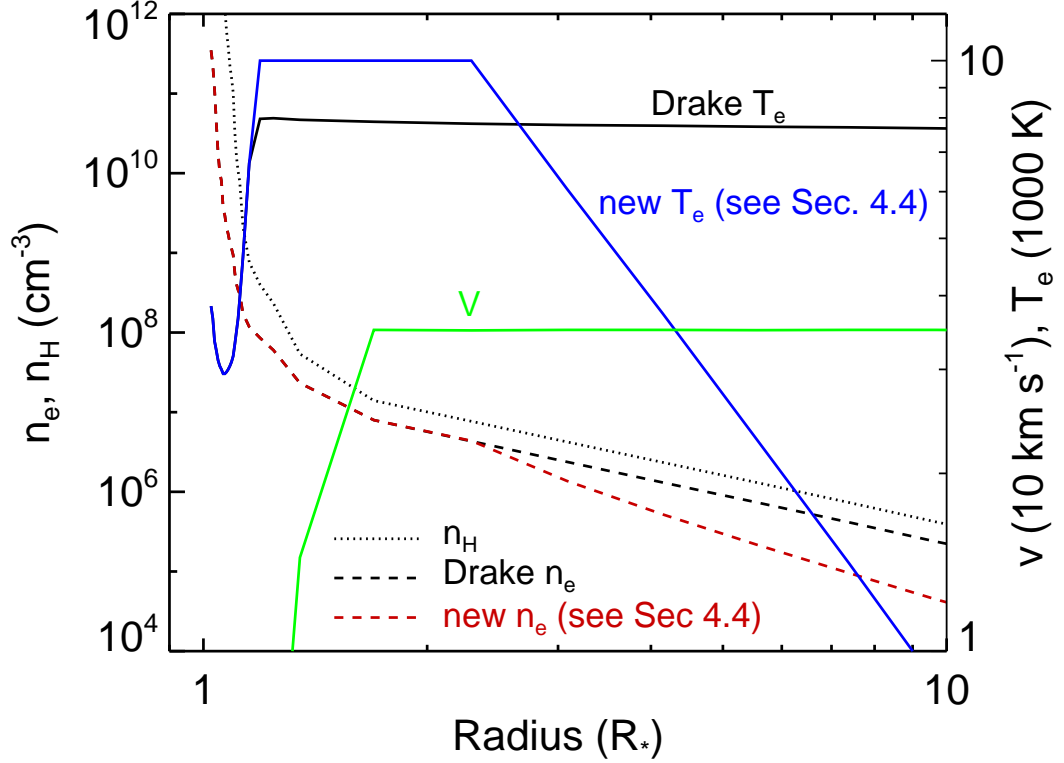


Figure 6.5: Existing atmospheric model for α Boo (Drake, 1985, ‘model A’) along with the same model which undergoes rapid wind cooling beyond $\sim 2.3 R_*$. The original Drake Model’s have a temperature plateau of $\sim 8,000 \text{ K}$ between 1.2 and $\sim 20 R_*$ (solid black line), reach a terminal velocity of $35 - 40 \text{ km s}^{-1}$ within $2 R_*$ (solid green line), and have a wind which is 50% ionized (dashed and dotted black lines).



A Nice Appendix

This is where the appendix would go...

References

- AIRAPETIAN, V., CARPENTER, K.G. & OFMAN, L. (2010). Winds from Luminous Late-type Stars. II. Broadband Frequency Distribution of Alfvén Waves. *Astrophysical Journal*, **723**, 1210–1218. (Cited on page 50.)
- ALTENHOFF, W.J., HUCHTMEIER, W.K., SCHMIDT, J., SCHRAML, J.B. & STUMPF, P. (1986). Radio continuum observations of comet Halley. *Astronomy & Astrophysics*, **164**, 227–230. (Cited on page 49.)
- ALTENHOFF, W.J., THUM, C. & WENDKER, H.J. (1994). Radio emission from stars: A survey at 250 GHz. *Astronomy & Astrophysics*, **281**, 161–183. (Cited on page 49.)
- AYRES, T.R. & LINSKY, J.L. (1975). Stellar model chromospheres. III - Arcturus /K2 III/. *Astrophysical Journal*, **200**, 660–674. (Cited on page 32.)
- AYRES, T.R., BROWN, A. & HARPER, G.M. (2003). Buried Alive in the Coronal Graveyard. *Astrophysical Journal*, **598**, 610–625. (Cited on pages 34 and 36.)
- BAADE, R., KIRSCH, T., REIMERS, D., TOUSSAINT, F., BENNETT, P.D., BROWN, A. & HARPER, G.M. (1996). The Wind Outflow of zeta Aurigae: A Model Revision Using Hubble Space Telescope Spectra. *Astrophysical Journal*, **466**, 979. (Cited on page 31.)
- BEASLEY, A.J., STEWART, R.T. & CARTER, B.D. (1992). Non-thermal radio emission from post-main-sequence stars. *Monthly Notices of the Royal Astronomical Society*, **254**, 1–6. (Cited on page 48.)
- BERIO, P., MERLE, T., THÉVENIN, F., BONNEAU, D., MOURARD, D., CHESNEAU, O., DELA, O., LIGI, R., NARDETTO, N., PERRAUT, K., PICHON, B., STEE, P., TALLON-BOSC, I., CLAUSSE, J.M., SPANG, A., MCALISTER, H., TEN BRUMMELAAR, T., STURMANN, J., STURMANN, L., TURNER, N., FARRINGTON, C. & GOLDFINGER, P.J. (2011). Chromosphere of K giant stars. Geometrical extent and spatial structure detection. *Astronomy & Astrophysics*, **535**, A59. (Cited on page 31.)
- BROWN, K.I.T. (2007). Long-Term Spectroscopic and Precise Radial Velocity Monitoring of Arcturus. *Publications of the Astronomical Society of the Pacific*, **119**, 237–237. (Cited on page 32.)
- BROWN, K.I.T., GRAY, D.F. & BALIUNAS, S.L. (2008). Long-Term Spectroscopic Monitoring of Arcturus. *Astrophysical Journal*, **679**, 1531–1540. (Cited on page 34.)
- CARPENTER, K.G. & ROBINSON, R.D. (1996). HST Studies of Carbon and K-M Giant/Supergiant Stars. In P. Benvenuti, F.D. Macchetto & E.J. Schreier, eds., *Science with the Hubble Space Telescope - II*, 418. (Cited on page 35.)

REFERENCES

- CARPENTER, K.G., ROBINSON, R.D., HARPER, G.M., BENNETT, P.D., BROWN, A. & MULLAN, D.J. (1999). GHRS Observations of Cool, Low-Gravity Stars. V. The Outer Atmosphere and Wind of the Nearby K Supergiant λ Velorum. *Astrophysical Journal*, **521**, 382–406. (Cited on page 31.)
- CASSINELLI, J.P. & HARTMANN, L. (1977). The effect of winds and coronae of hot stars on the infrared and radio continua. *Astrophysical Journal*, **212**, 488–493. (Cited on page 57.)
- CHAPMAN, R.D. (1981). The 1979-1980 eclipse of Zeta Aurigae. I - The circumstellar envelope. *Astrophysical Journal*, **248**, 1043–1052. (Cited on page 31.)
- COHEN, M., CARBON, D.F., WELCH, W.J., LIM, T., SCHULZ, B., MCMURRY, A.D., FORSTER, J.R. & GOORVITCH, D. (2005). Far-Infrared and Millimeter Continuum Studies of K Giants: α Bootis and α Tauri. *Astronomical Journal*, **129**, 2836–2848. (Cited on page 49.)
- CROWLEY, C., ESPEY, B.R. & MCCANDLISS, S.R. (2008). EG And: Far Ultraviolet Spectroscopic Explorer and Hubble Space Telescope STIS Monitoring of an Eclipsing Symbiotic Binary. *Astrophysical Journal*, **675**, 711–722. (Cited on page 31.)
- DECIN, L., VANDENBUSSCHE, B., WAELEKENS, C., DECIN, G., ERIKSSON, K., GUSTAFSSON, B., PLEZ, B. & SAUVAL, A.J. (2003). ISO-SWS calibration and the accurate modelling of cool-star atmospheres. IV. G9 to M2 stars. *Astronomy & Astrophysics*, **400**, 709–727. (Cited on pages 33 and 35.)
- DEHAES, S., BAUWENS, E., DECIN, L., ERIKSSON, K., RASKIN, G., BUTLER, B., DOWELL, C.D., ALI, B. & BLOMMAERT, J.A.D.L. (2011). Structure of the outer layers of cool standard stars. *Astronomy & Astrophysics*, **533**, A107. (Cited on pages 49 and 50.)
- DI BENEDETTO, G.P. (1993). Empirical effective temperatures and angular diameters of stars cooler than the sun. *Astronomy & Astrophysics*, **270**, 315–334. (Cited on pages 32 and 33.)
- DRAKE, S. & LINSKY, J. (1986). Radio continuum emission from winds, chromospheres, and coronae of cool giants and supergiants. *Astronomical Journal*, **91**, 602–620. (Cited on pages 48, 49, 50 and 55.)
- DRAKE, S.A. (1985). Modeling lines formed in the expanding chromospheres of red giants. In J.E. Beckman & L. Crivellari, eds., *Progress in stellar spectral line formation theory; Proceedings of the Advanced Research Workshop, Trieste, Italy, September 4-7, 1984 (A86-37976 17-90)*. Dordrecht, D. Reidel Publishing Co., 1985, p. 351–357. (Cited on pages 33, 34, 57, 61 and 64.)
- DRAKE, S.A. & LINSKY, J.L. (1983). First detection of winds in red giants by microwave continuum techniques. *Astrophysical Journal Letters*, **274**, L77–L81. (Cited on page 48.)
- DUPREE, A.K., LOBEL, A., YOUNG, P.R., AKE, T.B., LINSKY, J.L. & REDFIELD, S. (2005). A Far-Ultraviolet Spectroscopic Survey of Luminous Cool Stars. *Astrophysical Journal*, **622**, 629–652. (Cited on page 36.)
- DZIEMBOWSKI, W.A., GOUGH, D.O., HOUDEK, G. & SIENKIEWICZ, R. (2001). Oscillations of α UMa and other red giants. *Monthly Notices of the Royal Astronomical Society*, **328**, 601–610. (Cited on page 32.)

REFERENCES

- EATON, J.A. (2008). A Model for the Chromosphere/Wind of 31 Cygni and Its Implications for Single Stars. *Astronomical Journal*, **136**, 1964–1979. (Cited on page 31.)
- EGGEN, O.J. (1971). The Arcturus Group. *Publications of the Astronomical Society of the Pacific*, **83**, 271. (Cited on page 32.)
- EGGEN, O.J. (1996). Star Streams and Galactic Structure. *Astronomical Journal*, **112**, 1595. (Cited on page 32.)
- GLASSGOLD, A.E. & HUGGINS, P.J. (1986). The ionization structure of the circumstellar envelope of Alpha Orionis. *Astrophysical Journal*, **306**, 605–617. (Cited on pages 59 and 60.)
- GRAY, R.O., CORBALLY, C.J., GARRISON, R.F., MCFADDEN, M.T., BUBAR, E.J., MCGAHEE, C.E., O'DONOGHUE, A.A. & KNOX, E.R. (2006). Contributions to the Nearby Stars (NStars) Project: Spectroscopy of Stars Earlier than M0 within 40 pc-The Southern Sample. *Astronomical Journal*, **132**, 161–170. (Cited on page 33.)
- GRIFFIN, R.E.M. (1996). Arcturus and human evolution. *The Observatory*, **116**, 404–405. (Cited on page 32.)
- HARPER, G.M., BROWN, A., BENNETT, P.D., BAADE, R., WALDER, R. & HUMMEL, C.A. (2005). VLA Observations of ζ Aurigae: Confirmation of the Slow Acceleration Wind Density Structure. *Astronomical Journal*, **129**, 1018–1034. (Cited on page 31.)
- HARPER, G.M., O'RIAIN, N. & AYRES, T.R. (2013). Chromospheric thermal continuum millimetre emission from non-dusty K and M red giants. *Monthly Notices of the Royal Astronomical Society*, **428**, 2064–2073. (Cited on pages 31 and 50.)
- HARTMANN, L. & MACGREGOR, K.B. (1980). Momentum and energy deposition in late-type stellar atmospheres and winds. *Astrophysical Journal*, **242**, 260–282. (Cited on page 56.)
- HATZES, A.P. & COCHRAN, W.D. (1993). Long-period radial velocity variations in three K giants. *Astrophysical Journal*, **413**, 339–348. (Cited on pages 32, 33 and 35.)
- HATZES, A.P. & COCHRAN, W.D. (1998). On the nature of the radial velocity variability of Aldebaran - A search for spectral line bisector variations. *Monthly Notices of the Royal Astronomical Society*, **293**, 469. (Cited on page 35.)
- HÖGBOM, J.A. (1974). Aperture Synthesis with a Non-Regular Distribution of Interferometer Baselines. *Astronomy & Astrophysics Supplemental*, **15**, 417. (Cited on page 26.)
- JACKSON, N. (2008). Principles of Interferometry. In F. Bacciotti, L. Testi & E. Whelan, eds., *Jets from Young Stars II*, vol. 742 of *Lecture Notes in Physics*, Berlin Springer Verlag, 193. (Cited on pages 14 and 16.)
- KALLINGER, T., WEISS, W.W., BARBAN, C., BAUDIN, F., CAMERON, C., CARRIER, F., DE RIDDER, J., GOUPIL, M.J., GRUBERBAUER, M., HATZES, A., HEKKER, S., SAMADI, R. & DELEUIL, M. (2010). Oscillating red giants in the CoRoT exofield: asteroseismic mass and radius determination. *Astronomy & Astrophysics*, **509**, A77. (Cited on pages 32 and 33.)

REFERENCES

- KELCH, W.L., CHANG, S.H., FURENLID, I., LINSKY, J.L., BASRI, G.S., CHIU, H.Y. & MARAN, S.P. (1978). Stellar model chromospheres. VII - Capella /G5 III +/, Pollux /K0 III/, and Aldebaran /K5 III/. *Astrophysical Journal*, **220**, 962–979. (Cited on pages 35 and 36.)
- KRAUS, J.D., TIURI, M., RAISANEN, A.V. & CARR, T.D. (1986). *Radio astronomy receivers*. (Cited on page 5.)
- LACOUR, S., MEIMON, S., THIÉBAUT, E., PERRIN, G., VERHOELST, T., PEDRETTI, E., SCHULLER, P.A., MUGNIER, L., MONNIER, J., BERGER, J.P., HAUBOIS, X., PONCELET, A., LE BESNERAIS, G., ERIKSSON, K., MILLAN-GABET, R., RAGLAND, S., LACASSE, M. & TRAUB, W. (2008). The limb-darkened Arcturus: imaging with the IOTA/IONIC interferometer. *Astronomy & Astrophysics*, **485**, 561–570. (Cited on page 32.)
- LINSKY, J.L. & HAISCH, B.M. (1979). Outer atmospheres of cool stars. I - The sharp division into solar-type and non-solar-type stars. *Astrophysical Journal Letters*, **229**, L27–L32. (Cited on pages 34 and 35.)
- MASSAROTTI, A., LATHAM, D.W., STEFANIK, R.P. & FOGEL, J. (2008). Rotational and Radial Velocities for a Sample of 761 HIPPARCOS Giants and the Role of Binarity. *Astronomical Journal*, **135**, 209–231. (Cited on page 33.)
- MCMURRY, A.D. (1999). The outer atmosphere of Tau - I. A new chromospheric model. *Monthly Notices of the Royal Astronomical Society*, **302**, 37–47. (Cited on page 33.)
- MERLINE, W.J. (1999). Precise Velocity Observation of K-Giants: Evidence for Solar-Like Oscillations in Arcturus. In J.B. Hearnshaw & C.D. Scarfe, eds., *IAU Colloq. 170: Precise Stellar Radial Velocities*, vol. 185 of *Astronomical Society of the Pacific Conference Series*, 187. (Cited on page 32.)
- MICHELSON, A.A. (1890). . *Phil. Mag.*, **30**, 1–21. (Cited on page 20.)
- NAVARRO, J.F., HELMI, A. & FREEMAN, K.C. (2004). The Extragalactic Origin of the Arcturus Group. *Astrophysical Journal Letters*, **601**, L43–L46. (Cited on page 32.)
- O’GORMAN, E. & HARPER, G.M. (2011). What is Heating Arcturus’ Wind? In C. Johns-Krull, M.K. Browning & A.A. West, eds., *16th Cambridge Workshop on Cool Stars, Stellar Systems, and the Sun*, vol. 448 of *Astronomical Society of the Pacific Conference Series*, 691. (Cited on page 59.)
- OHNAKA, K. (2013). Spatially resolved, high-spectral resolution observation of the K giant Aldebaran in the CO first overtone lines with VLTI/AMBER. *Astronomy & Astrophysics*, **553**, A3. (Cited on page 50.)
- OLNON, F.M. (1975). Thermal bremsstrahlung radiospectra for inhomogeneous objects, with an application to MWC 349. *Astronomy & Astrophysics*, **39**, 217–223. (Cited on page 53.)
- PANAGIA, N. & FELLI, M. (1975). The spectrum of the free-free radiation from extended envelopes. *Astronomy & Astrophysics*, **39**, 1–5. (Cited on page 53.)

REFERENCES

- PERRYMAN, M.A.C., LINDEGREN, L., KOVALEVSKY, J., HOEG, E., BASTIAN, U., BERNACCA, P.L., CRÉZÉ, M., DONATI, F., GRENON, M., GREWING, M., VAN LEEUWEN, F., VAN DER MAREL, H., MIGNARD, F., MURRAY, C.A., LE POOLE, R.S., SCHRIJVER, H., TURON, C., ARENOU, F., FROESCHLÉ, M. & PETERSEN, C.S. (1997). The HIPPARCOS Catalogue. *Astronomy & Astrophysics*, **323**, L49–L52. (Cited on pages 32 and 33.)
- PROTHERO, D. & BUELL, C. (2007). *Evolution: what the fossils say and why it matters*. Columbia University Press. (Cited on page 1.)
- RAMÍREZ, I. & ALLENDE PRIETO, C. (2011). Fundamental Parameters and Chemical Composition of Arcturus. *Astrophysical Journal*, **743**, 135. (Cited on pages 32 and 33.)
- RETTET, A., BEDDING, T.R., BUZASI, D.L., KJELDSSEN, H. & KISS, L.L. (2003). Oscillations in Arcturus from WIRE Photometry. *Astrophysical Journal Letters*, **591**, L151–L154. (Cited on page 32.)
- RICCHICI, A. & ROCCATAGLIATA, V. (2005). Aldebaran’s angular diameter: How well do we know it? *Astronomy & Astrophysics*, **433**, 305–312. (Cited on page 33.)
- ROBINSON, R.D., CARPENTER, K.G. & BROWN, A. (1998). Goddard High-Resolution Spectrograph Observations of Cool Low-Gravity Stars. IV. A Comparison of the K5 III Stars alpha Tauri and gamma Draconis. *Astrophysical Journal*, **503**, 396. (Cited on pages 33, 35 and 57.)
- RYDE, N., LAMBERT, D.L., RICHTER, M.J. & LACY, J.H. (2002). Detection of Water Vapor in the Photosphere of Arcturus. *Astrophysical Journal*, **580**, 447–458. (Cited on page 34.)
- SAGAN, C. (1997). *The Demon-Haunted World: Science as a Candle in the Dark*. Ballantine Books. (Cited on page 1.)
- SEAQUIST, E.R. & TAYLOR, A.R. (1987). A detailed analysis of the radio emission from the symbiotic star RX Puppis. *Astrophysical Journal*, **312**, 813–821. (Cited on page 53.)
- SENNHAUSER, C. & BERDYUGINA, S.V. (2011). First detection of a weak magnetic field on the giant Arcturus: remnants of a solar dynamo? *Astronomy & Astrophysics*, **529**, A100. (Cited on pages 33 and 34.)
- SLEE, O.B., STEWART, R.T., BUNTON, J.D., BEASLEY, A.J., CARTER, B.D. & NELSON, G.J. (1989). A microwave survey of southern red giants. *Monthly Notices of the Royal Astronomical Society*, **239**, 913–922. (Cited on page 48.)
- SODERHJELM, S. & MIGNARD, F. (1998). Arcturus as a double star. *The Observatory*, **118**, 365–366. (Cited on page 32.)
- SPITZER, L. (1978). *Physical processes in the interstellar medium*. New York Wiley-Interscience, 1978. 333 p. (Cited on pages 62 and 63.)
- TAYLOR, G.B., CARILLI, C.L. & PERLEY, R.A., eds. (1999). *Synthesis Imaging in Radio Astronomy II*, vol. 180 of *Astronomical Society of the Pacific Conference Series*. (Cited on pages 9 and 10.)

REFERENCES

- TSUJI, T. (2008). Cool luminous stars: the hybrid nature of their infrared spectra. *Astronomy & Astrophysics*, **489**, 1271–1289. (Cited on page 35.)
- TSUJI, T. (2009). The K giant star Arcturus: the hybrid nature of its infrared spectrum. *Astronomy & Astrophysics*, **504**, 543–559. (Cited on page 34.)
- TURNER, N.H., TEN BRUMMELAAR, T.A. & MASON, B.D. (1999). Adaptive Optics Observations of Arcturus using the Mount Wilson 100 Inch Telescope. *Publications of the Astronomical Society of the Pacific*, **111**, 556–558. (Cited on page 32.)
- VAN LEEUWEN, F. (2007). Validation of the new Hipparcos reduction. *Astronomy & Astrophysics*, **474**, 653–664. (Cited on page 33.)
- WIEDEMANN, G., AYRES, T.R., JENNINGS, D.E. & SAAR, S.H. (1994). Carbon Monoxide Fundamental Bands in Late-Type Stars. III. Chromosphere or CO-mosphere? *Astrophysical Journal*, **423**, 806. (Cited on pages 34 and 36.)
- WILLIAMS, M.E.K., FREEMAN, K.C., HELMI, A. & RAVE COLLABORATION (2009). The Arcturus Moving Group: Its Place in the Galaxy. In J. Andersen, Nordströara, B. m & J. Bland-Hawthorn, eds., *IAU Symposium*, vol. 254 of *IAU Symposium*, 139–144. (Cited on page 32.)
- WOOD, B.E., HARPER, G.M., MÜLLER, H.R., HEERIKHUISEN, J. & ZANK, G.P. (2007). The Wind-ISM Interaction of α Tauri. *Astrophysical Journal*, **655**, 946–957. (Cited on pages 36, 49, 50 and 55.)
- WRIGHT, A.E. & BARLOW, M.J. (1975). The radio and infrared spectrum of early-type stars undergoing mass loss. *Monthly Notices of the Royal Astronomical Society*, **170**, 41–51. (Cited on page 53.)
- WRIGHT, K.O. (1970). The Zeta Aurigae stars. *Vistas in Astronomy*, **12**, 147–182. (Cited on page 31.)